

Intrinsic (Axion) Statistical Topological Insulator

Xi Chen,^{1,*} Fa-Jie Wang,^{1,*} Zhen Bi,² and Zhi-Da Song^{1,3,4,†}

¹International Center for Quantum Materials, School of Physics, Peking University, Beijing 100871, China

²Department of Physics, The Pennsylvania State University, University Park, Pennsylvania 16802, USA

³Hefei National Laboratory, Hefei 230088, China

⁴Collaborative Innovation Center of Quantum Matter, Beijing 100871, China

(Dated: January 3, 2025)

Ensembles that respect symmetries on average exhibit richer topological states than those in pure states with exact symmetries, leading to the concept of average symmetry-protected topological states (ASPTs). The fermion counterpart of ASPT is the so-called statistical topological insulator (STI) in disordered ensembles. In this work, we demonstrate the existence of *intrinsic* STI - which has no band insulator correspondence - characterized by the half-quantized magneto-electric polarization $P_3 = \theta/(2\pi)$. A C_4T symmetry reverses the sign of θ angle, hence seems to protect a \mathbb{Z}_2 classification of $\theta = 0, \pi$. However, we prove that, if $(C_4T)^4 = 1$, the topological state with $\theta = \pi$ cannot be realized in band insulators where C_4T is exact. Surprisingly, using a real space construction (topological crystal), we find that an STI with $\theta = \pi$ can arise in Anderson insulators with disorders respecting C_4T on average. To illustrate this state, we construct a lattice model and examine its phase diagram using the transfer matrix method up to the largest numerically accessible system size. An STI phase is identified through delocalized surface states and a half-quantized magneto-electric polarization in the bulk. As expected, an unavoidable gapless phase separates the STI from both clean insulators and trivial Anderson insulators, revealing the intrinsic nature of the STI. Moreover, we argue that the intrinsic STI is *robust* against electron-electron interactions, *i.e.*, interactions cannot open an adiabatic path connecting the STI to a gapped clean system. Thus, our work provides the first intrinsic crystalline ASPT and its lattice realization. We also generalize the discussion to other crystalline symmetries.

Introduction. Topological insulators (TIs) [1–5], including topological crystalline insulators (TCIs) [6–10], are band insulators that are not adiabatically connected to atomic limits without breaking the protecting symmetry [11–14]. Their classification in clean systems has been well established in various schemes [15–26]. For TIs protected by local symmetries, disorder, as an inevitable effect in realistic materials, does not change the classifications, provided the disorder respects the protecting symmetries [16, 17, 27]. Surprisingly, Refs. [28–30] showed that for some TIs protected by local or crystalline symmetries, even when disorder breaks the protecting symmetries, the TIs can remain robust, as long as the disorder respects the symmetries on *average*. Such TIs were later conceptually clarified in Ref. [31] and were termed as statistical TIs (STIs). An STI is defined as an ensemble of disordered systems that manifest robust, delocalized boundary states, which are pinned at critical points by the average symmetries. A symmetry is said exact if every element in the ensemble respects it, and said average if the ensemble as a whole is invariant under the symmetry, though individual elements may break it. The disorder is always assumed short-range correlated, hence each element is self-averaging in the thermodynamic limit. As noted in Refs. [31, 32], all the known examples of STIs are adiabatically connected to clean TIs when the disorders are turned off, and the average symmetry becomes exact. We hence call them *extrinsic* STIs.

A closely related concept to STIs is the average symmetry-protected topological (ASPT) phase [33], which has recently gained attentions. ASPT phase is the many-body counterpart

of STI. An intriguing discovery is the *intrinsic* ASPT phase [34] that cannot be adiabatically connected to a clean symmetric system with a gap. Basing on this observation, we introduce and explore the concept of *intrinsic* STI referring to topological phases only realizable in strongly disordered insulators.

The 3D \mathbb{Z}_2 TI protected by time-reversal symmetry (T) exhibits a topological magneto-electric effect described by the lagrangian term $\mathcal{L}_\theta = \frac{\theta e^2}{4\pi^2\hbar} \mathbf{E} \cdot \mathbf{B}$ with $\theta = \pi$ [35, 36]. If T is broken, other θ -odd symmetries, such as inversion [9, 36–39], roto-reflections [40–43], translation followed by T [7, 44], and rotations ($C_{n=2,3,4,6}$) followed by T [44–50], will also quantize θ to 0 or π . It is therefore generally believed that these symmetries can protect TCIs with $\theta = \pi$, known as axion TIs. However, counterintuitively, we find that a C_4T symmetry, which satisfies $(C_4T)^4 = 1$, *cannot* protect a $\theta = \pi$ state *unless* strong disorders leading to Anderson localization are introduced. (Note that such a C_4T can protect fragile topological band insulators [6, 44, 51], which have no stable surface state.) Our discovery marks the first example of intrinsic STI, highlighting a new type of topological phases.

Extrinsic axion STI. To begin, we first consider an extrinsic axion STI protected by an average inversion symmetry [52, 53]. If trivial local states are allowed to be added, clean TCIs can be adiabatically deformed to “topological crystals” [21, 22, 24], which consists of building blocks made up of lower-dimensional TIs, where the electron correlation length is much smaller than the lattice constant. The simplest topological crystal for an inversion-protected axion TI is illustrated in Fig. 1(a), where all the planes at integer (half-integer) z -coordinates are decorated with insulators with Chern number $C = 1$ (-1). The cubic with unit length represents the unit cell. Each unit cell has eight inversion centers at $x, y, z = 0, \frac{1}{2}$.

* These authors contribute equally to this work.

† songzd@pku.edu.cn

One can see that all the inversion centers in the system have been occupied by Chern insulators.

Now, we examine the spatial dependence of the local axion angle θ in the topological crystal by analyzing the magneto-electric response $\mathcal{P} = \frac{\theta}{2\pi} \frac{e}{\Phi_0} \mathbf{B}$ [35, 36], where $\Phi_0 = h/e$ is the flux quantum. Suppose the 3D block above (below) the considered Chern insulator has an axion angle θ_1 (θ_2), and its volume is given by $V_1 = S \cdot L_1$ ($V_2 = S \cdot L_2$), where S represents the area of the Chern insulator. Then, under a perpendicular magnetic field of strength B , the electric charge accumulated on the Chern insulator is given by

$$\Delta Q = -\frac{P_1 V_1}{L_1} + \frac{P_2 V_2}{L_2} = \frac{\theta_2 - \theta_1}{2\pi} \frac{e}{\Phi_0} B S. \quad (1)$$

On the other hand, there must be $\Delta Q = C \frac{e}{\Phi_0} B S$ according to the Streda formula of quantum Hall states [54], where C is the Chern number. The two expressions of ΔQ together imply $\theta_1 - \theta_2 = -2\pi C$, meaning that a variation of $\pm 2\pi$ in θ corresponds to crossing a Chern insulator with $C = \mp 1$. Within each 3D block embedded between two Chern insulators, θ must remain constant, as there is no electric response inside the region.

Since $\theta = 0$ in the vacuum, the value of θ in each 3D block in Fig. 1(a) is uniquely determined to be either 0 or 2π . Therefore, the average axion angle $\bar{\theta} = \pi$, provided that the distances between adjacent Chern insulators are equal, as required by the inversion symmetry. Note that a global change of -2π in θ can be realized by introducing a Chern bubble at the boundary (by creating and adding the dashed planes in Fig. 1(a)), which does not affect the bulk physics. This indicates that $\bar{\theta} \bmod 2\pi$ is a \mathbb{Z}_2 topological invariant.

We further demonstrate that θ is always single-valued in insulating topological crystals, ensuring that the average $\bar{\theta}$ is well-defined. In a general topological crystal, including the C_4T -symmetric state discussed below, a closed loop in space may cross multiple Chern insulators, as illustrated in Fig. 1(b). For the system to be insulating, the chiral edge modes of these Chern insulators must be locally gapped at the hinge where the Chern insulators intersect. This condition enforces that the net chirality (of chiral edge modes) enclosed by the loop to be zero, meaning that θ undergoes an equal number of changes of $\pm 2\pi$ around the loop. A $2n\pi$ winding of θ would correspond to n unpaired chiral modes enclosed by the loop, which should not appear in an insulating TCI.

Topological crystals for axion TIs are robust against weak quenched disorder respecting an average θ -odd symmetry. First, intra-Chern-layer disorders do not alter the topology of individual Chern layers as long as they are below the critical value for the Quantum Hall transition, ensuring that θ remains well-defined and single-valued. Second, inter-Chern-layer disorders may induce local fluctuations of θ by effectively changing distances between layers with opposite Chern numbers. Nevertheless, the average θ -odd symmetry still guarantees $\bar{\theta} = \pi$, as demonstrated in Ref. [52].

It has been shown that C_4T , as a θ -odd symmetry, can protect a higher-order TI characterized by $\bar{\theta} = \pi$ provided $(C_4T)^4 = -1$ [45, 50]. This state corresponds to the topological crystal shown in Fig. 1(c), (d), comprising four types

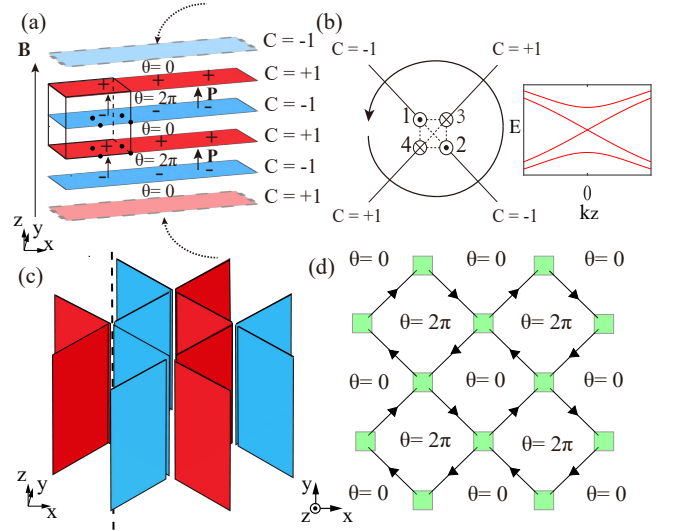


FIG. 1. (a) The simplest topological crystal for an inversion-protected axion TI. The box shows a unit cell, and the black dots show inversion centers. Red (blue) planes show Chern insulators with $C = 1(-1)$ with orientation $+z$. θ is the local axion angle. (b) A closed loop in an insulating topological crystal must enclose chiral modes with zero net chirality, ensuring that θ is single-valued. On a C_4T -symmetric hinge in (c), if $(C_4T)^4 = 1$, the $(C_4T)^2 = -1$ subspace hosts Kramer helical states, while the $(C_4T)^2 = 1$ subspace can be locally gapped, as shown by the 1D band structure on the right hand side. (c) A C_4T -symmetric topological crystal, where all C_4T axes are occupied by intersecting hinges of Chern layers. Red (blue) planes are Chern insulators with $C = 1(-1)$ with normal $(\mathbf{e}_x \pm \mathbf{e}_y)/\sqrt{2}$. (d) shows the local axion angle of each 3D block embedded between Chern insulators in (c), viewed from the $+z$ direction. The arrows show chiral modes on the z surface, separating 2D blocks with $C = \pm 1/2$.

of Chern layer blocks with normal vectors $(\mathbf{e}_x + \mathbf{e}_y)/\sqrt{2}$, $(\mathbf{e}_x - \mathbf{e}_y)/\sqrt{2}$, $(-\mathbf{e}_x + \mathbf{e}_y)/\sqrt{2}$, $(-\mathbf{e}_x - \mathbf{e}_y)/\sqrt{2}$ respectively, each with a Chern number of one along its normal. These blocks are connected via an array of C_4T axes, at each of which four Chern layers intersect and cyclically transform under C_4T symmetry. Each axis hosts two chiral edge modes propagating along \mathbf{e}_z and two anti-chiral edge modes propagating along $-\mathbf{e}_z$ (Fig. 1(b)). Assuming sufficiently large Chern gaps, the bulk low-energy physics of the topological crystal arises from these edge modes. Since the net chirality is zero, one may expect a symmetric gap to be allowed at each axis. This expectation holds true if $(C_4T)^4 = -1$, as demonstrated in Refs. [55, 56], leading to a gapped topological crystal that realizes the clean axion TI.

Intrinsic axion STI. For $(C_4T)^4 = 1$, a symmetric gap is forbidden in the clean limit, ruling out the clean axion TI. Consider the four edge modes at a C_4T axis, labeled as 1, 2, 3, 4 (Fig. 1(b)). Without loss of generality, we assume 1, 2 and 3, 4 are chiral and anti-chiral, respectively. C_4T transforms these modes as $1 \rightarrow 4 \rightarrow 2 \rightarrow 3 \rightarrow 1$. Since $(C_4T)^4 = 1$, the 4D Hilbert space splits into two 2D subspaces with $C_2 = (C_4T)^2$ eigenvalues ± 1 . The $C_2 = -1$ subspace is spanned by $\frac{1}{\sqrt{2}}(|1\rangle - |2\rangle)$ and $\frac{1}{\sqrt{2}}(|3\rangle - |4\rangle)$, which

have opposite chirality and form a Dirac point at $k_z = 0$. Since $(C_4T)^2 = -1$ in this subspace, the Kramers' degeneracy protects the Dirac point from being gapped. In contrast, the $C_2 = 1$ subspace, with $(C_4T)^2 = 1$, lacks Kramers' degeneracy and can be gapped. Thus, the absence of clean axion TI arises from Kramers' degeneracy in the $C_2 = -1$ subspace. In Ref. [56], following the topological crystal approach, we further show that C_4T satisfying $(C_4T)^4 = 1$ does not protect any clean (stable) TI.

In addition to the topological crystal argument, we also mathematically proved $\theta = 0 \pmod{2\pi}$ in C_4T -symmetric band insulators with $(C_4T)^4 = 1$. The magneto-electric polarization $P_3 = \theta/(2\pi)$ [3, 35] can be expressed through the winding number of the C_4T sewing matrix [41, 45, 50]

$$2P_3 = \int \frac{d^3\mathbf{k}}{24\pi^2} \epsilon_{ijk} \text{Tr} \left[(B\partial_i B^\dagger)(B\partial_j B^\dagger)(B\partial_k B^\dagger) \right] \pmod{2}. \quad (2)$$

Here $\partial_i \equiv \partial_{k_i}$, $B_{mn}(\mathbf{k}) = \langle u_m(C_4T \cdot \mathbf{k}) | C_4T | u_n(\mathbf{k}) \rangle$ is the C_4T sewing matrix, and $|u_{m,n}(\mathbf{k})\rangle$ are Bloch states of occupied bands. Since the winding number of $B(\mathbf{k})$ is an integer, P_3 is quantized to 0 or $1/2 \pmod{1}$, corresponding to trivial and axion insulators, respectively. We find that the winding number must be *even* if $(C_4T)^4 = 1$, which enforces $P_3 = 0$. The proof is sketched here, with details in Ref. [56]. The occupied bands can be adiabatically deformed into disconnected one-band blocks (which contribute trivially to Eq. (2)) and two-band blocks. Each two-band block realizes a mapping from the Brillouin zone (\mathbb{T}^3) to $SU(2)$, and its contribution to Eq. (2) is the degree of mapping, *i.e.*, how many times it wraps $SU(2)$. When $(C_4T)^4 = 1$, there exists a reference point in $SU(2)$ that the mapping must hit an even number of times, ensuring an even winding number.

To realize the *intrinsic* STI, we introduce Gaussian disorder with variance W at the hinges where Chern layers cross. This breaks the exact C_4T symmetry but preserves it on average. Since the bulk's low-energy physics is quasi-1D, a small W can localize the system without affecting the topology of the Chern layers, as disorder is confined to hinges. The local axion angle θ of each 3D block between Chern layers can be determined as in Fig. 1(d), following the method we did for Fig. 1(a). The average θ over 3D blocks is π . In the clean limit, θ is ill-defined around metallic helical modes, but with disorder, θ becomes well-defined and single-valued everywhere as the helical modes localize. Thus, the disordered topological crystal behaves as an Anderson insulator with $\bar{\theta} = \pi$, protected by the average C_4T symmetry.

dered topological crystal behaves as an Anderson insulator with $\bar{\theta} = \pi$, protected by the average C_4T symmetry.

Bulk-boundary correspondence. The nontrivial topology of the disordered topological crystal also manifests itself as delocalized surface states. Specifically, consider the surface in the z direction. Chiral edge modes emerge at the boundaries of Chern layers, forming a network structure. As shown in Fig. 1(d), they resemble Chalker's model that describes the quantum Hall transition [57]. To draw an analogy with the quantum Hall transition, we assign effective Chern numbers (C 's) to the 2D blocks on the surface. First, C 's of two adjacent surface 2D blocks differ by ± 1 , as they are separated by a chiral mode. These blocks represent the surfaces of adjacent 3D bulk blocks with $\theta = 0, 2\pi$. Second, the C_4T symmetry, which exchanges the two types of blocks, imposes that their C 's must be opposite. Thus, we assign effective Chern numbers $C = \pm 1/2$ to the two types of surface 2D blocks. The chiral modes can then be interpreted as domain walls between regions with $C = 1/2$ and $-1/2$. In the clean limit, the chiral modes connect to the bulk helical modes at the C_4T axes represented by green squares. However, in the presence of disorders that localize bulk states, the green squares represent scattering nodes with random strengths and phase shifts. The average C_4T symmetry ensures that regions with $C = 1/2, -1/2$ occupy equal areas. This symmetry condition pins the surface state at the critical point of the quantum Hall transition, where chiral modes percolate between $C = \pm 1/2$ regions and remain delocalized.

A lattice model. Inspired by the topological crystal, we now construct a lattice model for the intrinsic STI. A pair of chiral modes on opposite edges of a Chern insulator can be regularized to a wire of lattice: $2tk_z\sigma_z \rightarrow t\sin k_z\sigma_z + 2t(1 - \cos k_z)\sigma_x + m\sigma_x$, where $\sigma_z = \pm 1$ represents the chiral and anti-chiral modes around $k_z = 0$, and the mass term $m\sigma_x$ mimics a coupling between the two edges. If the Chern layer reaches thermodynamic limit within one unit cell, there must be $m = 0$. Here we use m as a tuning parameter. As will be shown below, a finite m drives the system away from the quasi-1D limit. Applying this regularization to the four Chern layers in the unit cell (Fig. 1(c)), we obtain an eight-band model shown in Fig. 2(a). Each pair of nearest neighbors in the xy plane form a wire that simulates a Chern layer. The red (γ) and dashed blue (λ) bonds represent couplings between the chiral and anti-chiral modes around the C_4T axes. The Hamiltonian is

$$H = \sum_{k_z, i} \zeta_i 2t \sin(k_z) c_{k_z, i}^\dagger c_{k_z, i} + \sum_{k_z, \langle i, j \rangle} (m + 2t(1 - \cos k_z)) c_{k_z, i}^\dagger c_{k_z, j} + \sum_{k_z, \langle\langle i, j \rangle\rangle} \gamma c_{k_z, i}^\dagger c_{k_z, j} + \sum_{k_z, \langle\langle\langle i, j \rangle\rangle\rangle} \lambda c_{k_z, i}^\dagger c_{k_z, j} \quad (3)$$

where i, j label sites in xy plane, $\zeta_i = 1, -1$ for white (chiral) and black (anti-chiral) sites respectively, and $\langle \cdot \rangle, \langle\langle \cdot \rangle\rangle, \langle\langle\langle \cdot \rangle\rangle\rangle$ represent first, second, and third nearest neighbor pairs, respectively. The model respects a C_4T symmetry satisfying

$(C_4T)^4 = 1$, which transforms the eight orbitals as $1 \rightarrow 3 \rightarrow 4 \rightarrow 2 \rightarrow 1, 5 \rightarrow 7 \rightarrow 8 \rightarrow 6 \rightarrow 5$. Even all the parameters are real, the time-reversal symmetry is inherently broken as chiral and anti-chiral modes from the same wire are coupled

to different C_4T centers. In Ref. [56] we find all the crystalline symmetries of this model, including a PT symmetry that squares to 1. In the following we focus on the state at half-filling. For $m = 0$, the model's low energy physics consists of decoupled 1D helical modes, as we have explained in the topological crystal argument, and the entire $k_z = 0$ plane lies on the Fermi surface. For $0 < |m| < 2\gamma$, the model is a nodal line semi-metal protected by PT (Fig. 2(b)). For $|m| > 2\gamma$, the system becomes a trivial band insulator.

Disorder is introduced by adding random imaginary components, $i\gamma'$, to the hopping γ along the red bonds. The random variables γ' follows Gaussian distribution with a variant W . γ' s on different bonds are assumed uncorrelated. The C_4T symmetry is preserved on average because it maps one disorder configuration to another with equal probability, leaving the disorder ensemble invariant.

Phase diagram. The disordered lattice model is studied using the transfer matrix method in a quasi-1D geometry [57–59], where the longitudinal size M (along the x direction) is much larger than the transverse size $L \times L$ (along the y and z directions). To study the localization of bulk states, we impose periodic boundary conditions along the y and z directions. The localization length $\xi_{1D}(L)$ along the longitudinal direction, which depends on L , is obtained from the Lyapunov exponents of the transfer matrix. The normalized quasi-1D localization length $\Lambda(L) = \xi_{1D}(L)/L$ characterizes the (de)localization behavior: etallic, critical, and localized states correspond to $\lim_{L \rightarrow \infty} \Lambda(L)$ being divergent, finite, and vanishing, respectively.

On the insulating side of a metal-insulator phase transition, the 3D localization length ξ_{3D} diverges as $|r - r_c|^{-\nu}$, where r is the tuning parameter, r_c is the critical value, and $\nu > 0$ is a universal exponent. $\Lambda(r, L)$ follows the one-parameter scaling law with the scaling variable L/ξ_{3D} for sufficiently large L [59]. For small L , an irrelevant correction to Λ due to the finite-size effect must be considered, and Λ takes the following form [60]:

$$\Lambda(r, L) = F(u_1(\tilde{r})L^{1/\nu}, u_2(\tilde{r})L^y) \quad (4)$$

where $\tilde{r} = (r - r_c)/r_c$, $y < 0$, and F, u_1, u_2 are undetermined functions that can be Taylor expanded near the phase transition point. The phase diagram in Fig. 2(d) is obtained by fitting Eq. (4) to numerically computed Λ . For example, in the insulator-metal transition shown in Fig. 2(c), we use W as the tuning parameter, and keep all other Hamiltonian parameters fixed. We obtain $W_c = 1.125$ [1.015, 1.162] and $\nu = 1.40$ [1.24, 1.56], which is consistent with previously reported value $\nu = 1.443$ [1.437, 1.449] for 3D Anderson transitions in the unitary class [61]. Other points on the phase boundary are determined similarly by choosing $r = W$ or m . Further numerical details are provided in Ref. [56].

When $m = 0$, the bulk's low energy states are quasi-1D and can be localized by arbitrarily small disorder strength W . This corresponds to a localization transition occurring at $W_{c1}(0) = 0$. As will be discussed in the next paragraph, the resulting insulating phase is identified as the intrinsic STI. For sufficiently large W , the system evolves into a trivial Anderson insulator. This implies a delocalized phase transition

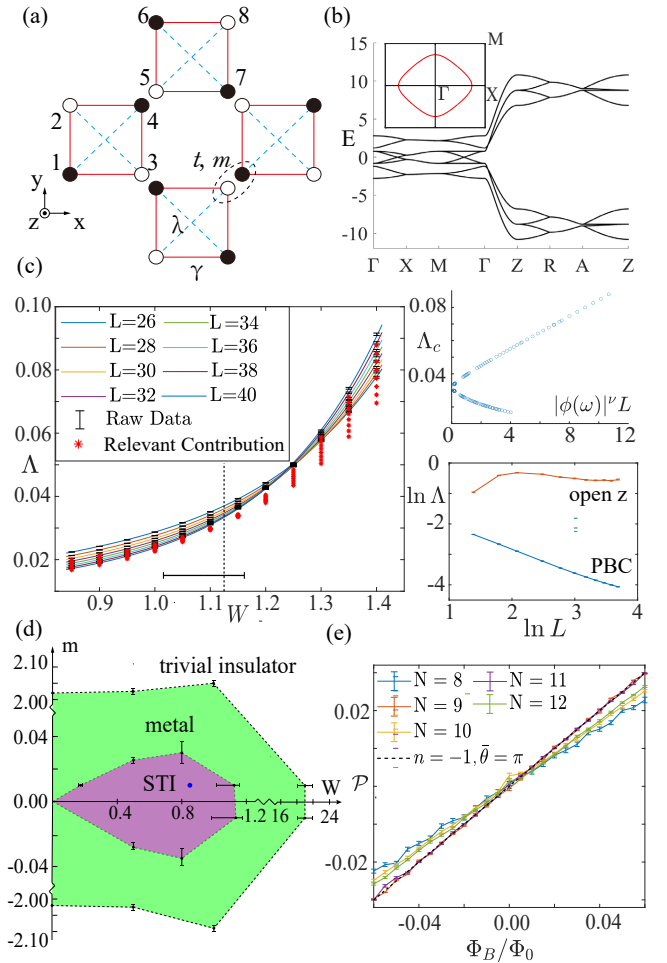


FIG. 2. (a) The lattice model viewed from the $+z$ direction. Red (blue) lines represent γ (λ). Black (white) circles represent chiral and anti-chiral modes. (b) Band structure of the lattice model with $t = 2, \gamma = 1, \lambda = 0.01$ and $m = 0.8$. Inset shows the nodal line on the $k_z = 0$ plane. (c) Numerical normalized quasi-1D localization length Λ with $t = 2, \gamma = 1, \lambda = 0.01, m = 0.01$ and the Fermi energy $E_F = -0.01$. Left: Raw data and polynomial fitting of Λ near $W_c \approx 1.125$. Upper right: Collapse of the relevant contribution to Λ to a one-parameter scaling function. Lower right: Comparison of Λ with $W = 0.85$ between periodic boundary condition in y, z directions and open z boundary condition. (d) Phase diagram of the disordered lattice model with $t = 2, \gamma = 1, \lambda = 0.01$ and $E_F = -0.01$. The axion insulator phase (purple) is completely surrounded by a gapless phase (green), which is in turn surrounded by the trivial insulator phase (white). (e) The topological magnetoelectric response with $m = 0.01, W = 0.85$. Other parameters are the same as (d).

within the disorder range $[W_{c2}(0), W_{c3}(0)]$ that separates the STI from the trivial Anderson insulator. $W_{c2}(0)$ and $W_{c3}(0)$ are estimated as 1.12 and 20.0, respectively. When m is small but nonzero, the bulk becomes a nodal-line semi-metal [62]. As W increases, the system undergoes a localization transition at a finite $W_{c1}(m)$ [63–65], entering the STI phase. With further increase in W , the system experiences successive insulator-metal-insulator transitions at $W_{c2}(m)$ and $W_{c3}(m)$,

eventually reaching the trivial Anderson insulator phase. Notably, $W_{e1}(m)$ and $W_{e2}(m)$ merge at $m \approx \pm 0.03$, enclosing the intrinsic STI phase, which is separated from both the trivial Anderson insulator at $W \rightarrow \infty$ and clean insulators at $W = 0$.

Topological surface state. To demonstrate the delocalized surface state of the STI, we recalculate the normalized localization length $\Lambda'(L)$ under an open boundary condition in the z -direction. This setup allows us to observe surface-specific phenomena, which are otherwise hidden under periodic boundary conditions. As discussed in Fig. 1(d), the surface state is expected to exhibit quantum Hall criticality. Using the parameters corresponding to the blue point within the STI phase in Fig. 2(d), we find that $\Lambda'(L)$ indeed exhibits critical behavior - it remains constant as L approaches infinity. This behavior is in sharp contrast to the result under periodic boundary conditions, where $\Lambda(L)$ decays with L and reveals localization, as shown in Fig. 2(c).

Topological magneto-electric effect. To further illustrate the nontrivial topology of the intrinsic STI, we directly compute the magneto-electric response of the disordered lattice model in a cubic geometry with N^3 sites. Periodic boundary condition is imposed along the z direction to avoid delocalized surface states, while open boundary conditions are applied along x and y directions. A magnetic field B is introduced along the x direction, and the resulting electric polarization is measured as $\mathcal{P} = \langle \hat{X} \rangle / N^3$, where $\langle \hat{X} \rangle$ is the expectation value of the x -coordinate for occupied states. Theoretically, \mathcal{P} is given by $-(n + P_3)\Phi_B/\Phi_0$ where Φ_B is the flux through a unit cell, n is a surface-dependent integer, and $P_3 = \bar{\theta}/(2\pi)$ represents the magneto-electric polarization. The disorder-averaged \mathcal{P} (over 100 configurations) is plotted as a function of B in Fig. 2(e). The slope $d\mathcal{P}/(d\Phi_B/\Phi_0)$ converges to $\frac{1}{2}$ as N increases, confirming the topological magneto-electric effect characterized by $P_3 = \frac{1}{2}$.

Discussions. Based on topological crystal theory, winding number analysis in momentum space, numerical determination of localization length and topological magneto-electric effect, our work demonstrated the existence of intrinsic STI - a new topological phase that has no band insulator correspondence. Furthermore, we argue that the STI is a well-defined intrinsic fermion ASPT even in the presence of electron-electron interactions. Within the topological crystal framework, an intrinsic ASPT is characterized by an obstruction to block decoration, where the system cannot be symmetrically gapped even with interactions, in the absence of disorder. However, the introduction of statistically symmetric disorder enables localization, leading to a short-range entangled bulk, while the boundary remains delocalized. In our case, the decorated Chern insulators around a C_4T axis generate one-dimensional hinge modes exhibiting a $U(1)$ and C_4T mixed anomaly, preventing a symmetric gap from forming even with interactions. By breaking C_4T symmetry down to an average symmetry through disorder, the anomaly constraint is lifted, allowing these modes to become localized and rendering the system's ground states short-range correlated. Indeed, the disordered 1D hinge problem maps to the boundary of a 2D topological insulator with average time-reversal symmetry, where boundary states are known to localize in the presence of interactions [66]. Thus, the topological crystal construction still realizes the same intrinsic STI even with interactions present.

In Ref. [56], we also generalize the discussions to a C_2T symmetry squaring to -1 .

Acknowledgments. We are grateful to Yang Qi and Rui-Xing Zhang for helpful discussions. Z.-D. S., X. C., and F.-J. W. were supported by National Natural Science Foundation of China (General Program No. 12274005), National Key Research and Development Program of China (No. 2021YFA1401900), and Innovation Program for Quantum Science and Technology (No. 2021ZD0302403). Z. B. acknowledges support from NSF under award number DMR-2339319.

-
- [1] C. L. Kane and E. J. Mele, “ \mathbb{Z}_2 topological order and the quantum spin hall effect,” *Phys. Rev. Lett.* **95**, 146802 (2005).
 - [2] B. Andrei Bernevig, Taylor L. Hughes, and Shou-Cheng Zhang, “Quantum spin hall effect and topological phase transition in hgte quantum wells,” *Science* **314**, 1757–1761 (2006).
 - [3] Liang Fu, C. L. Kane, and E. J. Mele, “Topological insulators in three dimensions,” *Phys. Rev. Lett.* **98**, 106803 (2007).
 - [4] M. Z. Hasan and C. L. Kane, “Colloquium: Topological insulators,” *Rev. Mod. Phys.* **82**, 3045–3067 (2010).
 - [5] Xiao-Liang Qi and Shou-Cheng Zhang, “Topological insulators and superconductors,” *Rev. Mod. Phys.* **83**, 1057–1110 (2011).
 - [6] Liang Fu, “Topological crystalline insulators,” *Phys. Rev. Lett.* **106**, 106802 (2011).
 - [7] Roger S. K. Mong, Andrew M. Essin, and Joel E. Moore, “Antiferromagnetic topological insulators,” *Phys. Rev. B* **81**, 245209 (2010).
 - [8] Ari M. Turner, Yi Zhang, and Ashvin Vishwanath, “Entanglement and inversion symmetry in topological insulators,” *Phys. Rev. B* **82**, 241102 (2010).
 - [9] Taylor L. Hughes, Emil Prodan, and B. Andrei Bernevig, “Inversion-symmetric topological insulators,” *Phys. Rev. B* **83**, 245132 (2011).
 - [10] Chao-Xing Liu, Rui-Xing Zhang, and Brian K. VanLeeuwen, “Topological nonsymmorphic crystalline insulators,” *Phys. Rev. B* **90**, 085304 (2014).
 - [11] Alexey A. Soluyanov and David Vanderbilt, “Wannier representation of \mathbb{Z}_2 topological insulators,” *Physical Review B* **83**, 035108 (2011).
 - [12] Barry Bradlyn, Luis Elcoro, Jennifer Cano, Maia G Vergniory, Zhijun Wang, Claudia Felser, Mois I Aroyo, and B Andrei Bernevig, “Topological quantum chemistry,” *Nature* **547**, 298–305 (2017).
 - [13] Hoi Chun Po, Ashvin Vishwanath, and Haruki Watanabe, “Symmetry-based indicators of band topology in the 230 space groups,” *Nature communications* **8**, 50 (2017).
 - [14] Jorrit Kruthoff, Jan De Boer, Jasper Van Wezel, Charles L Kane, and Robert-Jan Slager, “Topological classification of crystalline insulators through band structure combinatorics,”

- Physical Review X* **7**, 041069 (2017).
- [15] Alexei Kitaev, “Periodic table for topological insulators and superconductors,” *AIP Conference Proceedings* **1134**, 22–30 (2009).
- [16] Andreas P. Schnyder, Shinsei Ryu, Akira Furusaki, and Andreas W. W. Ludwig, “Classification of topological insulators and superconductors in three spatial dimensions,” *Phys. Rev. B* **78**, 195125 (2008).
- [17] Shinsei Ryu, Andreas P. Schnyder, Akira Furusaki, and Andreas W. W. Ludwig, “Topological insulators and superconductors: tenfold way and dimensional hierarchy,” *New Journal of Physics* **12**, 065010 (2010).
- [18] Ching-Kai Chiu, Hong Yao, and Shinsei Ryu, “Classification of topological insulators and superconductors in the presence of reflection symmetry,” *Phys. Rev. B* **88**, 075142 (2013).
- [19] Ken Shiozaki, Masatoshi Sato, and Kiyonori Gomi, “ Z_2 topology in nonsymmorphic crystalline insulators: Möbius twist in surface states,” *Phys. Rev. B* **91**, 155120 (2015).
- [20] Ken Shiozaki, Masatoshi Sato, and Kiyonori Gomi, “Topology of nonsymmorphic crystalline insulators and superconductors,” *Phys. Rev. B* **93**, 195413 (2016).
- [21] Hao Song, Sheng-Jie Huang, Liang Fu, and Michael Hermele, “Topological Phases Protected by Point Group Symmetry,” *Physical Review X* **7**, 011020 (2017).
- [22] Sheng-Jie Huang, Hao Song, Yi-Ping Huang, and Michael Hermele, “Building crystalline topological phases from lower-dimensional states,” *Phys. Rev. B* **96**, 205106 (2017).
- [23] Eslam Khalaf, Hoi Chun Po, Ashvin Vishwanath, and Haruki Watanabe, “Symmetry indicators and anomalous surface states of topological crystalline insulators,” *Phys. Rev. X* **8**, 031070 (2018).
- [24] Zhida Song, Sheng-Jie Huang, Yang Qi, Chen Fang, and Michael Hermele, “Topological states from topological crystals,” *Science Advances* **5**, eaax2007 (2019).
- [25] Eyal Cornfeld and Adam Chapman, “Classification of crystalline topological insulators and superconductors with point group symmetries,” *Phys. Rev. B* **99**, 075105 (2019).
- [26] Ken Shiozaki, “The classification of surface states of topological insulators and superconductors with magnetic point group symmetry,” *Progress of Theoretical and Experimental Physics* **2022**, 04A104 (2022).
- [27] Jian Li, Rui-Lin Chu, J. K. Jain, and Shun-Qing Shen, “Topological anderson insulator,” *Phys. Rev. Lett.* **102**, 136806 (2009).
- [28] Liang Fu and C. L. Kane, “Topology, Delocalization via Average Symmetry and the Symplectic Anderson Transition,” *Phys. Rev. Lett.* **109**, 246605 (2012).
- [29] Zohar Ringel, Yaacov E. Kraus, and Ady Stern, “Strong side of weak topological insulators,” *Physical Review B* **86**, 045102 (2012).
- [30] Roger S. K. Mong, Jens H. Bardarson, and Joel E. Moore, “Quantum transport and two-parameter scaling at the surface of a weak topological insulator,” *Phys. Rev. Lett.* **108**, 076804 (2012).
- [31] I. C. Fulga, B. van Heck, J. M. Edge, and A. R. Akhmerov, “Statistical topological insulators,” *Phys. Rev. B* **89**, 155424 (2014), Average symmetry is referred to as statistical symmetry in this work.
- [32] Adam Yanis Chaou, Mateo Moreno-Gonzalez, Alexander Altland, and Piet W Brouwer, “Disordered topological crystalline phases,” *arXiv preprint arXiv:2412.01883* (2024).
- [33] Ruochen Ma and Chong Wang, “Average symmetry-protected topological phases,” *Phys. Rev. X* **13**, 031016 (2023).
- [34] Ruochen Ma, Jian-Hao Zhang, Zhen Bi, Meng Cheng, and Chong Wang, “Topological phases with average symmetries: the decohered, the disordered, and the intrinsic,” *arXiv preprint arXiv:2305.16399* (2023).
- [35] Xiao-Liang Qi, Taylor L. Hughes, and Shou-Cheng Zhang, “Topological field theory of time-reversal invariant insulators,” *Phys. Rev. B* **78**, 195424 (2008).
- [36] Zhong Wang, Xiao-Liang Qi, and Shou-Cheng Zhang, “Equivalent topological invariants of topological insulators,” *New Journal of Physics* **12**, 065007 (2010).
- [37] Ari M. Turner, Yi Zhang, Roger S. K. Mong, and Ashvin Vishwanath, “Quantized response and topology of magnetic insulators with inversion symmetry,” *Phys. Rev. B* **85**, 165120 (2012).
- [38] Eslam Khalaf, “Higher-order topological insulators and superconductors protected by inversion symmetry,” *Phys. Rev. B* **97**, 205136 (2018).
- [39] Sander H. Kooi, Guido van Miert, and Carmine Ortix, “Inversion-symmetry protected chiral hinge states in stacks of doped quantum hall layers,” *Phys. Rev. B* **98**, 245102 (2018).
- [40] Andrew M. Essin, Joel E. Moore, and David Vanderbilt, “Magnetoelectric polarizability and axion electrodynamics in crystalline insulators,” *Phys. Rev. Lett.* **102**, 146805 (2009).
- [41] Chen Fang, Matthew J. Gilbert, and B. Andrei Bernevig, “Bulk topological invariants in noninteracting point group symmetric insulators,” *Phys. Rev. B* **86**, 115112 (2012).
- [42] Dániel Varjas, Fernando de Juan, and Yuan-Ming Lu, “Bulk invariants and topological response in insulators and superconductors with nonsymmorphic symmetries,” *Phys. Rev. B* **92**, 195116 (2015).
- [43] Guido van Miert and Carmine Ortix, “Higher-order topological insulators protected by inversion and rotoinversion symmetries,” *Phys. Rev. B* **98**, 081110 (2018).
- [44] Rui-Xing Zhang and Chao-Xing Liu, “Topological magnetic crystalline insulators and corepresentation theory,” *Physical Review B* **91**, 115317 (2015).
- [45] Frank Schindler, Ashley M. Cook, Maia G. Vergniory, Zhijun Wang, Stuart S. P. Parkin, B. Andrei Bernevig, and Titus Neupert, “Higher-order topological insulators,” *Science Advances* **4**, eaat0346 (2018).
- [46] Nicodemos Varnava and David Vanderbilt, “Surfaces of axion insulators,” *Phys. Rev. B* **98**, 245117 (2018).
- [47] Benjamin J Wieder and B Andrei Bernevig, “The axion insulator as a pump of fragile topology,” *arXiv preprint arXiv:1810.02373* (2018).
- [48] Motohiko Ezawa, “Magnetic second-order topological insulators and semimetals,” *Phys. Rev. B* **97**, 155305 (2018).
- [49] Junyeong Ahn and Bohm-Jung Yang, “Symmetry representation approach to topological invariants in $C_{2z}T$ -symmetric systems,” *Phys. Rev. B* **99**, 235125 (2019).
- [50] Heqiu Li and Kai Sun, “Pfaffian formalism for higher-order topological insulators,” *Phys. Rev. Lett.* **124**, 036401 (2020).
- [51] A. Alexandradinata, J. Höller, Chong Wang, Hengbin Cheng, and Ling Lu, “Crystallographic splitting theorem for band representations and fragile topological photonic crystals,” *Phys. Rev. B* **102**, 115117 (2020).
- [52] Zhi-Da Song, Biao Lian, Raquel Queiroz, Roni Ilan, B. Andrei Bernevig, and Ady Stern, “Delocalization transition of a disordered axion insulator,” *Phys. Rev. Lett.* **127**, 016602 (2021).
- [53] Hailong Li, Hua Jiang, Chui-Zhen Chen, and X. C. Xie, “Critical behavior and universal signature of an axion insulator state,” *Phys. Rev. Lett.* **126**, 156601 (2021).
- [54] P Štefeda, “Theory of quantised hall conductivity in two dimensions,” *Perspectives in Condensed Matter Physics* **2**, 161–165 (1982).
- [55] Bingrui Peng, Yi Jiang, Zhong Fang, Hongming Weng, and

- Chen Fang, “Topological classification and diagnosis in magnetically ordered electronic materials,” *Phys. Rev. B* **105**, 235138 (2022).
- [56] “See Supplemental Materials at . . . for supplementary data and technical details.”
- [57] JT Chalker and PD Coddington, “Percolation, quantum tunnelling and the integer hall effect,” *Journal of Physics C: Solid State Physics* **21**, 2665 (1988).
- [58] Jean-Louis Pichard and G Sarma, “Finite size scaling approach to anderson localisation,” *Journal of Physics C: Solid State Physics* **14**, L127 (1981).
- [59] A. MacKinnon and B. Kramer, “One-parameter scaling of localization length and conductance in disordered systems,” *Phys. Rev. Lett.* **47**, 1546–1549 (1981).
- [60] Keith Slevin and Tomi Ohtsuki, “Corrections to scaling at the anderson transition,” *Phys. Rev. Lett.* **82**, 382–385 (1999).
- [61] Keith Slevin and Tomi Ohtsuki, “Estimate of the critical exponent of the anderson transition in the three and four-dimensional unitary universality classes,” *Journal of the Physical Society of Japan* **85**, 104712 (2016).
- [62] A. A. Burkov, M. D. Hook, and Leon Balents, “Topological nodal semimetals,” *Physical Review B* **84**, 235126 (2011).
- [63] Xunlong Luo, Baolong Xu, Tomi Ohtsuki, and Ryuichi Shindou, “Critical behavior of anderson transitions in three-dimensional orthogonal classes with particle-hole symmetries,” *Phys. Rev. B* **101**, 020202 (2020).
- [64] KX Jia, XY Liu, R Ma, H Geng, L Sheng, and DY Xing, “Phase diagram of three dimensional disordered nodal-line semimetals: weak localization to anderson localization,” *New Journal of Physics* **25**, 113033 (2023).
- [65] Miguel Gonçalves, Pedro Ribeiro, Eduardo V. Castro, and Miguel A. N. Araújo, “Disorder-driven multifractality transition in weyl nodal loops,” *Phys. Rev. Lett.* **124**, 136405 (2020).
- [66] Yang-Zhi Chou, Rahul M. Nandkishore, and Leo Radzihovsky, “Gapless insulating edges of dirty interacting topological insulators,” *Phys. Rev. B* **98**, 054205 (2018).
- [67] H. B. Nielsen and M. Ninomiya, “Absence of neutrinos on a lattice: (II). Intuitive topological proof,” *Nuclear Physics B* **193**, 173–194 (1981).
- [68] H. B. Nielsen and M. Ninomiya, “Absence of neutrinos on a lattice: (I). Proof by homotopy theory,” *Nuclear Physics B* **185**, 20–40 (1981).
- [69] Luis Elcoro, Benjamin J. Wieder, Zhida Song, Yuanfeng Xu, Barry Bradlyn, and B. Andrei Bernevig, “Magnetic topological quantum chemistry,” *Nature Communications* **12**, 5965 (2021).
- [70] Victor Guillemin and Alan Pollack, *Differential topology*, Vol. 370 (American Mathematical Soc., 2010).
- [71] S. V. Gallego, E. S. Tasci, G. de la Flor, J. M. Perez-Mato, and M. I. Aroyo, “Magnetic symmetry in the Bilbao Crystallographic Server: a computer program to provide systematic absences of magnetic neutron diffraction,” *Journal of Applied Crystallography* **45**, 1236–1247 (2012), number: 6 Publisher: International Union of Crystallography.
- [72] J. M. Perez-Mato, S. V. Gallego, E. S. Tasci, L. Elcoro, G. de la Flor, and M. I. Aroyo, “Symmetry-Based Computational Tools for Magnetic Crystallography,” *Annual Review of Materials Research* **45**, 217–248 (2015), publisher: Annual Reviews.
- [73] Valery Iustinovich Oseledec, “A multiplicative ergodic theorem, lyapunov characteristic numbers for dynamical systems,” *Transactions of the Moscow Mathematical Society* **19**, 197–231 (1968).

Appendix

Contents

References	5
A. Absence of clean axion insulator ($(C_4T)^4 = 1$): Momentum space proof	9
1. P_3 and the winding number of sewing matrix	9
2. Trivial P_3	10
3. Complexity from C_2 sewing matrix	14
B. Topological crystal	17
C. The lattice model	20
1. Model and symmetry	20
2. Low energy states	23
3. Random fluxes or imaginary hoppings	25
4. Uniform C_4T -breaking flux patterns	26
D. Numerical methods and results	27
1. Quasi-1D localization length and the transfer matrix method	27
2. Scaling analysis and Polynomial fitting of Λ	28
3. Numerical results	29
E. Generalization to $(C_2T)^2 = -1$ symmetry	31

A. Absence of clean axion insulator $((C_4T)^4 = 1)$: Momentum space proof

In this section, we prove that a C_4T -symmetric band insulator must have a vanishing magneto-electric polarization P_3 if $(C_4T)^4 = 1$.

1. P_3 and the winding number of sewing matrix

In a band insulator, the magneto-electric polarization $P_3 = \frac{\theta}{2\pi}$ can be calculated as a Chern-Simons integral [3, 35]

$$P_3 = \frac{1}{16\pi^2} \int d^3\mathbf{k} \epsilon_{ijk} \text{Tr} \left[\left(\mathcal{F}^{ij}(\mathbf{k}) - \frac{2}{3} i \mathcal{A}^i(\mathbf{k}) \mathcal{A}^j(\mathbf{k}) \right) \mathcal{A}^k(\mathbf{k}) \right] \pmod{1}. \quad (\text{A1})$$

where the indices $i, j, k = x, y, z$ are implicitly summed when repeated, ϵ_{ijk} is the Levi-Civita symbol. The non-Abelian Berry connection and curvature are defined as

$$\mathcal{A}_{mn}^i(\mathbf{k}) = -i \langle u_m(\mathbf{k}) | \partial_i | u_n(\mathbf{k}) \rangle, \quad \mathcal{F}^{ij} = \partial_i \mathcal{A}^j - \partial_j \mathcal{A}^i + i [\mathcal{A}^i, \mathcal{A}^j], \quad (\text{A2})$$

respectively, where $\partial_i \equiv \partial_{k_i}$. One should not confuse the minus sign in \mathcal{A}^i . The band indices m, n are limited to the occupied bands. Upon a gauge transformation within occupied bands $|u_n(\mathbf{k})\rangle \rightarrow |u_l(\mathbf{k})\rangle U_{nl}^*(\mathbf{k})$, where repeated band indices are implicitly summed, the Berry connection and curvature transform as

$$\mathcal{A}^i \rightarrow U \mathcal{A}^i U^\dagger - i U \partial_i U^\dagger, \quad \mathcal{F}^{ij} \rightarrow U \mathcal{F}^{ij} U^\dagger, \quad (\text{A3})$$

respectively. Substituting the gauge transformation into Eq. (A1), we obtain the change of the integral

$$\begin{aligned} \Delta P_3 = & \frac{1}{16\pi^2} \int d^3\mathbf{k} \epsilon_{ijk} \text{Tr} \left[\frac{2}{3} (U^\dagger \partial_i U) (U^\dagger \partial_j U) (U^\dagger \partial_k U) + i \mathcal{F}^{ij} (U^\dagger \partial_k U) + \frac{2}{3} \mathcal{A}^i \mathcal{A}^j (U^\dagger \partial_k U) + \frac{2}{3} (U^\dagger \partial_i U) \mathcal{A}^j \mathcal{A}^k \right. \\ & \left. + \frac{2}{3} \mathcal{A}^i (U^\dagger \partial_j U) \mathcal{A}^k + \frac{2i}{3} (U^\dagger \partial_i U) (U^\dagger \partial_j U) \mathcal{A}^k + \frac{2i}{3} \mathcal{A}^i (U^\dagger \partial_j U) (U^\dagger \partial_k U) + \frac{2i}{3} (U^\dagger \partial_i U) \mathcal{A}^j (U^\dagger \partial_k U) \right]. \quad (\text{A4}) \end{aligned}$$

Using the cyclic condition of trace, we simplify it to

$$\Delta P_3 = \frac{1}{16\pi^2} \int d^3\mathbf{k} \epsilon_{ijk} \text{Tr} \left[\frac{2}{3} (U^\dagger \partial_i U) (U^\dagger \partial_j U) (U^\dagger \partial_k U) + i \mathcal{F}^{ij} (U^\dagger \partial_k U) + 2 \mathcal{A}^i \mathcal{A}^j (U^\dagger \partial_k U) - 2i \mathcal{A}^j (\partial_k U^\dagger) (\partial_i U) \right]. \quad (\text{A5})$$

Expanding \mathcal{F}^{ij} in terms of the Berry connection, we find that the last three terms in the above equation sum to a full derivative term

$$\begin{aligned} & \frac{1}{16\pi^2} \int d^3\mathbf{k} \epsilon_{ijk} \text{Tr} \left[2i (\partial_i \mathcal{A}^j) (U^\dagger \partial_k U) - 2 \mathcal{A}^i \mathcal{A}^j (U^\dagger \partial_k U) + 2 \mathcal{A}^i \mathcal{A}^j (U^\dagger \partial_k U) + 2i \mathcal{A}^j (\partial_i U^\dagger) (\partial_k U) \right] \\ & = \frac{1}{16\pi^2} \int d^3\mathbf{k} \epsilon_{ijk} \cdot \partial_i \cdot \text{Tr} [2i \mathcal{A}^j (U^\dagger \partial_k U)] = 0. \quad (\text{A6}) \end{aligned}$$

Then

$$\Delta P_3 = \frac{1}{24\pi^2} \int d^3\mathbf{k} \epsilon_{ijk} \text{Tr} [(U^\dagger \partial_i U) (U^\dagger \partial_j U) (U^\dagger \partial_k U)] \quad (\text{A7})$$

has the form of a 3D winding number, which is an integer. Therefore, P_3 defined in Eq. (A1) is a gauge invariant quantity after modulo 1.

Now let us see how P_3 is quantized by a C_4T symmetry. We do not specify $(C_4T)^4 = 1$ or -1 in this subsection.

The following derivation parallels that in Refs. [35, 41]. We define the C_4T sewing matrix as

$$B_{mn}(\mathbf{k}) = \langle u_m(C_4T \cdot \mathbf{k}) | C_4T | u_n(\mathbf{k}) \rangle, \quad (\text{A8})$$

where $C_4T \cdot \mathbf{k} = (k_y, -k_x, -k_z)$. It is direct to verify that $B_{mn}(\mathbf{k})$ is unitary and periodic over the Brillouin zone. It immediately follows

$$C_4T | u_n(\mathbf{k}) \rangle = | u_m(C_4T \cdot \mathbf{k}) \rangle \cdot B_{mn}(\mathbf{k}), \quad | u_m(C_4T \cdot \mathbf{k}) \rangle = B_{mn}^*(\mathbf{k}) \cdot C_4T \cdot | u_n(\mathbf{k}) \rangle, \quad (\text{A9})$$

where implicit summations over repeated band indices are limited to occupied bands. We write $C_4T \cdot \mathbf{k}$ as \mathbf{k}' for simplicity. The coordinate transformation has the form $k'_i = R_{ij}k_j$, with $R \cdot R^T = 1$, $\det R = -1$. The derivatives with respect to k (∂) and k' (∂') are related by $\partial_i = R_{ji}\partial'_j$, $\partial'_i = R_{ij}\partial_j$. The non-Abelian Berry connection defined in the new coordinate is

$$\begin{aligned} \tilde{\mathcal{A}}_{mn}^i(\mathbf{k}') &\equiv -i\langle u_m(\mathbf{k}') | \partial'_i | u_n(\mathbf{k}') \rangle = -i\langle u_m(\mathbf{k}') | R_{ij} \partial_j | u_n(\mathbf{k}') \rangle = -iR_{ij} B_{mm'}(\mathbf{k}) \langle C_4T \cdot u_{m'}(\mathbf{k}) | \partial_j [C_4T \cdot u_{n'}(\mathbf{k})] B_{nn'}^*(\mathbf{k}) \rangle \\ &= -iR_{ij} B_{mm'}(\mathbf{k}) \langle u_{m'}^*(\mathbf{k}) | \partial_j | u_{n'}(\mathbf{k}) \rangle B_{nn'}^*(\mathbf{k}) - iR_{ij} B_{ml}(\mathbf{k}) \partial_j B_{nl}^*(\mathbf{k}) \\ &= -R_{ij} [B(\mathbf{k}) \mathcal{A}^{j*}(\mathbf{k}) B^\dagger(\mathbf{k})]_{mn} - iR_{ij} [B(\mathbf{k}) \partial_j B^\dagger(\mathbf{k})]_{mn}. \end{aligned} \quad (\text{A10})$$

After a few steps of algebra, one can also derive

$$\tilde{\mathcal{F}}^{ij}(\mathbf{k}') \equiv \partial'_i \tilde{\mathcal{A}}^j(\mathbf{k}') - \partial'_j \tilde{\mathcal{A}}^i(\mathbf{k}') + i[\tilde{\mathcal{A}}^i(\mathbf{k}'), \tilde{\mathcal{A}}^j(\mathbf{k}')] = -R_{ii'} R_{jj'} B(\mathbf{k}) \mathcal{F}^{i'j'*}(\mathbf{k}) B^\dagger(\mathbf{k}). \quad (\text{A11})$$

Suppose

$$\begin{aligned} q + P_3 &= \frac{1}{16\pi^2} \int d^3\mathbf{k} \epsilon_{ijk} \text{Tr} \left[\left(\mathcal{F}^{ij}(\mathbf{k}) - \frac{2}{3} i \mathcal{A}^i(\mathbf{k}) \mathcal{A}^j(\mathbf{k}) \right) \mathcal{A}^k(\mathbf{k}) \right] \\ &= \frac{1}{16\pi^2} \int d^3\mathbf{k}' \epsilon_{ijk} \text{Tr} \left[\left(\tilde{\mathcal{F}}^{ij}(\mathbf{k}') - \frac{2}{3} i \tilde{\mathcal{A}}^i(\mathbf{k}') \tilde{\mathcal{A}}^j(\mathbf{k}') \right) \tilde{\mathcal{A}}^k(\mathbf{k}') \right]. \end{aligned} \quad (\text{A12})$$

The two rows are the same quantity expressed in two coordinate systems, hence they equal to each other. Here q is the gauge-dependent integer part of the integral, and P_3 ranges from 0 to 1. Inserting Eqs. (A10) and (A11) to the second expression, we obtain

$$q + P_3 = \frac{1}{16\pi^2} \int d^3\mathbf{k} \epsilon_{ijk} R_{ii'} R_{jj'} R_{kk'} \text{Tr} \left[\left(B \mathcal{F}^{i'j'*} B^\dagger + \frac{2i}{3} (B \mathcal{A}^{i'*} B^\dagger + i B \partial_{i'} B^\dagger) (B \mathcal{A}^{j'*} B^\dagger + i B \partial_{j'} B^\dagger) \right) (B \mathcal{A}^{k'*} B^\dagger + i B \partial_{k'} B^\dagger) \right]. \quad (\text{A13})$$

Since $\epsilon_{ijk} R_{ii'} R_{jj'} R_{kk'} = \det R \cdot \epsilon_{i'j'k'}$ and $\det R = -1$, the above equation becomes

$$\begin{aligned} q + P_3 &= -\frac{1}{16\pi^2} \int d^3\mathbf{k} \epsilon_{ijk} \text{Tr} \left[\left(B \mathcal{F}^{ij*} B^\dagger + \frac{2i}{3} (B \mathcal{A}^{i*} B^\dagger + i B \partial_i B^\dagger) (B \mathcal{A}^{j*} B^\dagger + i B \partial_j B^\dagger) \right) (B \mathcal{A}^{k*} B^\dagger + i B \partial_k B^\dagger) \right] \\ &= -\frac{1}{16\pi^2} \int d^3\mathbf{k} \epsilon_{ijk} \text{Tr} \left[\left(\mathcal{F}^{ij}(\mathbf{k}) - \frac{2}{3} i \mathcal{A}^i(\mathbf{k}) \mathcal{A}^j(\mathbf{k}) \right) \mathcal{A}^k(\mathbf{k}) \right]^* - \frac{1}{24\pi^2} \int d^3\mathbf{k} \epsilon_{ijk} \text{Tr} \left[(B \partial_i B^\dagger) (B \partial_j B^\dagger) (B \partial_k B^\dagger) \right] \\ &\quad - \frac{1}{16\pi^2} \int d^3\mathbf{k} \epsilon_{ijk} \text{Tr} \left[-i \mathcal{F}^{ij*} (B^\dagger \partial_k B) + \frac{2}{3} \mathcal{A}^{i*} \mathcal{A}^{j*} (B^\dagger \partial_k B) + \frac{2}{3} \mathcal{A}^{i*} (B^\dagger \partial_j B) \mathcal{A}^{k*} + \frac{2}{3} (B^\dagger \partial_i B) \mathcal{A}^{j*} \mathcal{A}^{k*} \right. \\ &\quad \left. - \frac{2i}{3} (B^\dagger \partial_i B) (B^\dagger \partial_j B) \mathcal{A}^{k*} - \frac{2i}{3} (B^\dagger \partial_i B) \mathcal{A}^{j*} (B^\dagger \partial_k B) - \frac{2i}{3} \mathcal{A}^{i*} (B^\dagger \partial_j B) (B^\dagger \partial_k B) \right]. \end{aligned} \quad (\text{A14})$$

The first term in the second row equals to $-q - P_3$. The complex conjugations of the last seven terms (in the third and fourth rows) share the same form as the last seven terms in Eq. (A4), which have been shown as a full derivative term. Then, there must be

$$2P_3 = -\frac{1}{24\pi^2} \int d^3\mathbf{k} \epsilon_{ijk} \text{Tr} \left[(B \partial_i B^\dagger) (B \partial_j B^\dagger) (B \partial_k B^\dagger) \right] \pmod{2}. \quad (\text{A15})$$

Since the integral on the right hand side is a 3D winding number (an integer), P_3 is either 0 or $\frac{1}{2} \pmod{1}$. Therefore, in the presence of a C_4T symmetry, regardless of $(C_4T)^4 = 1$ or -1 , P_3 can only take value 0 or $\frac{1}{2}$.

We have assumed a smooth $B(\mathbf{k})$ to validate the differentials in Eq. (A15). This can be fulfilled when the system does not exhibit 3D Chern numbers: For topological states protected by symmetries (translation excluded), one can always choose a symmetry-breaking Wannier gauge [11] where the states are smooth over the Brillouin zone.

2. Trivial P_3

In this subsection we prove $P_3 = 0$ if $(C_4T)^4 = 1$ by showing that the winding number on the right hand side of Eq. (A15) is always even. First, we block-diagonalize the C_4T sewing matrix B into two-by-two and one-by-one blocks. A one-by-one block always contributes zero to the winding number. Each two-by-two block B^r ($r = 1, 2, \dots$) realizes a mapping from the 3D torus T^3 to $SU(2) \sim S^3$ and contributes a factor $\text{deg}[B^r]$ - degree of the mapping- to the winding number [36, 50]. $\text{deg}[B^r]$ counts how many times the domain manifold (T^3) wraps around the target manifold $SU(2)$. One can choose a *regular* value

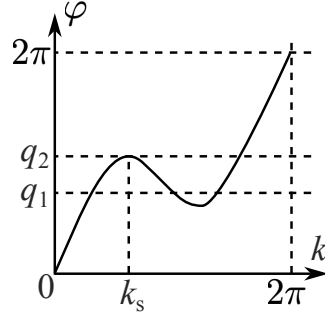


FIG. 3. A Map f from S^1 to S^1 . To calculate the parity of $\deg[f]$, one can choose a regular value, *e.g.*, q_1 , in the target manifold and count its preimages. The parity of the number of preimages gives $\deg[f] \bmod 2$. One should not use a critical value, *e.g.*, q_2 , for the counting.

$q_{\text{ref}} \in \text{SU}(2)$ and counts how many times q_{ref} is hit by the mapping B^r , as illustrated in Fig. 3. Parity of the counting gives $\deg[B^r] \bmod 2$, and hence determines P_3 . We will prove that, if $(C_4T)^4 = 1$, there exists such a q_{ref} that the counting is always even, implying $P_3 = 0$.

We introduce the sewing matrix for $C_2 = (C_4T)^2$

$$D_{mn}(\mathbf{k}) = \langle u_m(C_2\mathbf{k}) | C_2 | u_n(\mathbf{k}) \rangle. \quad (\text{A16})$$

$D(\mathbf{k})$ is unitary and periodic over the Brillouin zone. It is related to the C_4T sewing matrix via

$$D_{mn}(\mathbf{k}) = \langle u_m(C_2\mathbf{k}) | C_4T \cdot C_4T | u_n(\mathbf{k}) \rangle = \langle u_m(C_2\mathbf{k}) | C_4T \left[|u_l(C_4T \cdot \mathbf{k})\rangle B_{ln}(\mathbf{k}) \right] \rangle = [B(C_4T \cdot \mathbf{k}) B^*(\mathbf{k})]_{mn}, \quad (\text{A17})$$

where Eq. (A9) is inserted. Thus, the C_4T sewing matrix at $C_4T \cdot \mathbf{k}$ is related to that at \mathbf{k} by

$$B(C_4T \cdot \mathbf{k}) = D(\mathbf{k}) \cdot B^T(\mathbf{k}). \quad (\text{A18})$$

Applying this equation twice, we obtain

$$B(C_2 \cdot \mathbf{k}) = D(C_4T \cdot \mathbf{k}) \cdot B^T(C_4T \cdot \mathbf{k}) = D(C_4T \cdot \mathbf{k}) \cdot B(\mathbf{k}) \cdot D^T(\mathbf{k}). \quad (\text{A19})$$

For later convenience, we define the high symmetry momenta

$$\begin{aligned} \Gamma : (0, 0, 0), & \quad X : (\pi, 0, 0), & \quad Y : (0, \pi, 0), & \quad M : (\pi, \pi, 0) \\ Z : (0, 0, \pi), & \quad R : (\pi, 0, \pi), & \quad T : (0, \pi, \pi), & \quad A : (\pi, \pi, \pi). \end{aligned}$$

There are four C_2 -invariant high symmetry lines: ΓZ , XR , YT , MA . For \mathbf{k} belonging to these lines, $D(\mathbf{k})$ is a diagonal matrix consisting of C_2 eigenvalues. Since $C_2^2 = 1$, the C_2 eigenvalues can only be ± 1 . There are four C_4T -invariant high symmetry momenta $K^4 = \{\Gamma, M, Z, A\}$. For $\mathbf{k}_0 \in K^4$, the sewing matrix B must satisfy $B(\mathbf{k}_0) = D(\mathbf{k}_0) B^T(\mathbf{k}_0)$. A $D(\mathbf{k}_0) = -1$ eigenvalue must be at least doubly degenerate because the minimal $B(\mathbf{k}_0)$ matrix satisfying $B(\mathbf{k}_0) = -B^T(\mathbf{k}_0)$ is $e^{i\alpha} \sigma_y$, where α is an arbitrary phase factor. States at X or Y are generally non-degenerate, and there must be $D(X) = D^*(Y)$ according to Eq. (A19).

For simplicity, we assume there is no accidental degeneracy within the occupied bands. If an accidental degeneracy happens, we add a symmetry-allowed perturbation term to lift it. This operation does not change the value of P_3 of the occupied bands. (To be concrete, let us consider Weyl points between two nearby bands. According to the C_4T symmetry, the irreducible Brillouin zone is $\frac{1}{4}$ of the full Brillouin zone. Since the C_4T symmetry preserves the topological charges of Weyl points, the irreducible Brillouin zone and its C_4T partners must have the same charge. Thus, according to the Nielsen-Ninomiya theorem [67, 68], which guarantees a vanishing total topological charge in lattice models, the irreducible Brillouin zone must also have a zero topological charge. The irreducible Brillouin zone could have pairs of Weyl points with opposite charges, but one can design proper continuous deformation to annihilate them within the irreducible Brillouin zone.) The only remained degeneracies are the $D(\mathbf{k}_0) = -1$ states at $\mathbf{k}_0 \in K^4$. Then the occupied bands decompose into a set of disconnected groups, as shown in Fig. 4(a) and (b). The sewing matrices then have block-diagonal forms:

$$D(\mathbf{k}) = \bigoplus_r D^r(\mathbf{k}), \quad B(\mathbf{k}) = \bigoplus_r B^r(\mathbf{k}). \quad (\text{A20})$$

A 1D block must have $D^r(\Gamma, M) = 1$ such that no Kramer degeneracy appears. We then identify two types of 1D blocks in terms of C_2 eigenvalues

$$D^r(\Gamma) = 1, \quad D^r(M) = 1, \quad D^r(X) = \pm 1. \quad (\text{A21})$$

Similarly, there are nine types of 2D blocks in terms of C_2 eigenvalues:

$$D^r(\Gamma) = -\sigma_0, \quad D^r(M) = -\sigma_0, \quad D^r(X) = \sigma_0, -\sigma_0, \sigma_z, \quad (\text{A22})$$

$$D^r(\Gamma) = -\sigma_0, \quad D^r(M) = \sigma_0, \quad D^r(X) = \sigma_0, -\sigma_0, \sigma_z, \quad (\text{A23})$$

$$D^r(\Gamma) = \sigma_0, \quad D^r(M) = -\sigma_0, \quad D^r(X) = \sigma_0, -\sigma_0, \sigma_z. \quad (\text{A24})$$

There is no higher dimensional block. The blocks contribute to the winding number in Eq. (A15) independently. Since the C_2 symmetry does not protect any stable band topology [55, 69], and we are not considering 3D Chern insulators in this work, the C_2 sewing matrix $D(\mathbf{k})$ should take form of band representations (BRs) [12] - symmetry-allowed atomic limits - of the space group $P2$, or represent fragile topological states of $P2$. We will discuss the complexity from C_2 sewing matrix in Sec. A3 and for now only focus on the simplest \mathbf{k} -independent choices

$$D^r(\mathbf{k}) = 1, \quad D^r(\mathbf{k}) = -\sigma_0 \quad (\text{A25})$$

for 1D and 2D blocks, respectively. Since no block exhibits 3D Chern numbers, $B^r(\mathbf{k})$ can be smoothly defined over the Brillouin zone. We do *not* assume a diagonal structure of $B^r(\mathbf{k})$ on the energy eigenstates, which may lead to some singularities in $B^r(\mathbf{k})$.

We consider a U(1) gauge transformation to the r -th block: $|u'_n(\mathbf{k})\rangle = |u_n(\mathbf{k})\rangle e^{i\varphi(\mathbf{k})/d_r}$, where $\varphi(\mathbf{k})$ is smoothly defined over the Brillouin zone and $d_r = 1$ or 2 is the dimension of the r -th block. $\varphi(\mathbf{k})$ should exhibit even (if nonzero) winding numbers across the Brillouin zone for $d_r = 2$ to ensure the periodicity of $|u'_n(\mathbf{k})\rangle$. The C_4T and C_2 sewing matrices on the transformed basis are

$$B^{r'}(\mathbf{k}) = e^{-\frac{i}{d_r}(\varphi(C_4T \cdot \mathbf{k}) + \varphi(\mathbf{k}))} B^r(\mathbf{k}), \quad D^{r'}(\mathbf{k}) = e^{-\frac{i}{d_r}(\varphi(C_2 \cdot \mathbf{k}) - \varphi(\mathbf{k}))} D^r(\mathbf{k}), \quad (\text{A26})$$

respectively. The purpose of this gauge transformation will become clear in the next paragraph. We require $\varphi(C_2 \cdot \mathbf{k}) = \varphi(\mathbf{k})$ such that the constant D sewing matrices in Eq. (A25) remain unchanged under the transformation. If φ can be chosen to satisfy

$$i(\varphi(C_4T\mathbf{k}) + \varphi(\mathbf{k})) = \ln \det B^r(\mathbf{k}), \quad \varphi(C_2 \cdot \mathbf{k}) = \varphi(\mathbf{k}), \quad (\text{A27})$$

then $\det B^{r'}(\mathbf{k}) = 1$ and $D^{r'}(\mathbf{k}) = D^r(\mathbf{k})$ (Eq. (A25)) are fulfilled in the same gauge. We now examine whether there are topological obstructions to Eq. (A27):

- (i) Denote $\vartheta(\mathbf{k}) = \varphi(C_4T\mathbf{k}) + \varphi(\mathbf{k})$. As φ is smoothly defined over the Brillouin zone, $\vartheta(\mathbf{k})$ must have vanishing winding numbers on arbitrary contractable loops. $\ln \det B^r(\mathbf{k})$ must also have vanishing winding numbers on contractable loops as $B^r(\mathbf{k})$ is smoothly defined over the Brillouin zone (see discussions below Eq. (A15)).
- (ii) $\vartheta(\mathbf{k})$ must have vanishing winding number on the non-contractable loop $\mathcal{C}_z : (0, 0, -\pi) \rightarrow (0, 0, \pi)$ because $\vartheta(0, 0, k_z) = \vartheta(0, 0, -k_z)$ by definition. For the considered C_2 sewing matrices in Eq. (A25), Eq. (A18) implies $\det B^r(0, 0, k_z) = \det B^r(0, 0, -k_z)$, meaning $\ln \det B^r(\mathbf{k})$ also has vanishing winding number along \mathcal{C}_z .
- (iii) The winding numbers of $\vartheta(\mathbf{k})$ along non-contractable loops $\mathcal{C}_x : (-\pi, 0, 0) \rightarrow (\pi, 0, 0)$, $\mathcal{C}_y : (0, -\pi, 0) \rightarrow (0, \pi, 0)$ must be zero because $\vartheta(\mathbf{k}) = \vartheta(C_2 \cdot \mathbf{k})$ by definition. For the considered sewing matrices in Eq. (A25), Eq. (A18) also implies vanishing winding numbers of $\ln \det B^r(\mathbf{k})$ along $\mathcal{C}_{x,y}$.

Since there is no topological obstruction to Eq. (A27), one can find such a gauge where $\det B^{r'}(\mathbf{k}) = 1$ and $D^{r'}(\mathbf{k})$ is given by Eq. (A25). Moreover, as $\vartheta(\mathbf{k})$ has vanishing winding numbers along non-contractable loops, $B^{r'}(\mathbf{k})$ (Eq. (A26)) remains periodic over the Brillouin zone [36]. In the following we will stick to this gauge and relabel $B^{r'}(\mathbf{k})$, $D^{r'}(\mathbf{k})$ as $B^r(\mathbf{k})$, $D^r(\mathbf{k})$, respectively.

A 1D block always has $B^r(\mathbf{k}) = 1$ and hence contributes trivially to the winding number. For a 2D block, B^r realizes a mapping from $\text{BZ} \sim \text{T}^3$ to $\text{SU}(2) \sim \text{S}^3$. Then, the right hand side of Eq. (A15) reduces to [36, 50]

$$\sum_r \deg[B^r] \pmod{2} \quad (\text{A28})$$

with $\deg[B^r]$ being the degree of the mapping between oriented manifolds with the same dimension [70]. The degree can be computed via a simple counting

$$\deg[B^r] = \sum_{\mathbf{k} \in (B^{r-1})[q_{\text{ref}}]} \text{sgn}_{\mathbf{k}}[B^r]. \quad (\text{A29})$$

Here $q_{\text{ref}} \in \text{SU}(2)$ is a *regular value* of the mapping, meaning that at each preimage $\mathbf{k} \in (B^{r-1})[q_{\text{ref}}]$, the mapping has a full-rank Jacobian. (\mathbf{k} is a regular (critical) point if the local Jacobian is (not) full-rank, and its image is a regular (critical) value.) See Fig. 3 for example. $\text{sgn}_{\mathbf{k}}[B^r]$ is the sign of the Jacobian determinant, which equals to $+1$ (-1) if the local mapping around \mathbf{k} keeps (reverses) the orientation of the manifold. We need to choose a convenient reference point q_{ref} to evaluate Eq. (A28). We notice that Eq. (A18) and $D^r(\mathbf{k}) = -\sigma_0$ imply

$$\forall \mathbf{k}_0 \in K^4, \quad B^r(\mathbf{k}_0) = -B^{rT}(\mathbf{k}_0) \quad \Rightarrow \quad B^r(\mathbf{k}_0) = \pm i\sigma_y. \quad (\text{A30})$$

Let us first try the reference point $q_{\text{ref}} = i\sigma_y$. If there is $B^r(\mathbf{k}) = i\sigma_y$ for some $\mathbf{k} \notin K^4$, then there must be $B^r(C_4T \cdot \mathbf{k}) = -B^{rT}(\mathbf{k}) = i\sigma_y$. We can reasonably assume that such $\mathbf{k} \notin K^4$ are regular points where the Jacobian is full-rank: Even if \mathbf{k} was critical, the singularity is not enforced by symmetry and hence can be removed. In particular, a C_2 -symmetric momentum \mathbf{k}_1 must be critical. This follows from Eq. (A19) and $D^r(\mathbf{k}_1) = -\sigma_0$, which together imply that $B^r(\mathbf{k}_1 + \mathbf{p})$ must be even in p_x, p_y , leading to a vanishing Jacobian determinant at \mathbf{k}_1 . While $B^r(\mathbf{k}_1) = i\sigma_y$ could occur accidentally at a C_2 -symmetric $\mathbf{k}_1 \notin K^4$, we can avoid this by adding perturbation to the Hamiltonian or applying a gauge transformation to $B^r(\mathbf{k})$, moving the preimage of $i\sigma_y$ to one or more regular points in the neighborhood of \mathbf{k}_1 . Since this happens at \mathbf{k}_1 and $C_4T \cdot \mathbf{k}_1$ simultaneously, the contribution to $\deg[B^r]$ (Eq. (A29)) is always even. Thus, we only need to examine contributions from K^4 . A $\mathbf{k}_0 \in K^4$ is automatically C_2 -symmetric and hence critical. However, unlike other C_2 -symmetric points, if $\mathbf{k}_0 \in K^4$ is a preimage of $i\sigma_y$, one cannot continuously move the preimage to its neighborhood by a perturbation to the Hamiltonian or a gauge transformation because $B^r(\mathbf{k}_0)$ can only take discrete values $\pm i\sigma_y$ due to Eq. (A30). Nevertheless, we can perturbatively change the reference point q_{ref} such that \mathbf{k}_0 is no longer a preimage of the new q_{ref} . In the next two paragraphs we will show that \mathbf{k}_0 will split into an even number of regular preimages upon the change of q_{ref} , hence each \mathbf{k}_0 also contributes trivially to $\deg[B^r] \bmod 2$. Thus, $\deg[B^r] \bmod 2$ is always zero.

We parameterize $B^r(\mathbf{k})$ around a preimage $\mathbf{k}_0 \in K^4$ of $i\sigma_y$. Consider $\mathbf{k} = \mathbf{k}_0 + \mathbf{p}$ with \mathbf{p} being a small quantity, Eq. (A18) and $D^r(\mathbf{k}) = -\sigma_0$ imply

$$B^r(\mathbf{k}_0 + \mathbf{p}) = \sum_{\mu=0,x,y,z} d_{\mu}(\mathbf{p})\sigma_{\mu} = [\beta_{01}p_z + \beta_{02}(p_x^2 - p_y^2) + 2\beta_{03}p_xp_y]\sigma_0 + [\beta_{11}p_z + \beta_{12}(p_x^2 - p_y^2) + 2\beta_{13}p_xp_y]i\sigma_x \\ + [1 + \alpha_{21}p_z^2 + \alpha_{22}(p_x^2 + p_y^2)]i\sigma_y + [\beta_{31}p_z + \beta_{32}(p_x^2 - p_y^2) + 2\beta_{33}p_xp_y]i\sigma_z + \mathcal{O}(p^3), \quad (\text{A31})$$

where α, β are real coefficients. Since

$$B^{r\dagger}B^r = \sigma_0[1 + 2\alpha_{22}(p_x^2 + p_y^2) + (2\alpha_{21} + \beta_{01}^2 + \beta_{11}^2 + \beta_{31}^2)p_z^2] + \mathcal{O}(p^3). \quad (\text{A32})$$

The normalization condition requires $\alpha_{22} = 0$, $\alpha_{21} = -(\beta_{01}^2 + \beta_{11}^2 + \beta_{31}^2)/2$. Using $d_{0,x,z}$ as local coordinates for $\text{SU}(2)$, we obtain the Jacobian determinant

$$\left| \frac{\partial d_{0,x,z}}{\partial p_{x,y,z}} \right| = 4 \begin{vmatrix} \beta_{01} & \beta_{02} & \beta_{03} \\ \beta_{11} & \beta_{12} & \beta_{13} \\ \beta_{31} & \beta_{32} & \beta_{33} \end{vmatrix} \cdot (p_x^2 + p_y^2) + \mathcal{O}(p^3). \quad (\text{A33})$$

It vanishes at $\mathbf{p} = 0$.

We perturbatively move the reference point away from the critical value $i\sigma_y$:

$$q_{\text{ref}}(\varepsilon) = ie^{i\frac{\varepsilon}{2}\sigma_z}\sigma_y e^{-i\frac{\varepsilon}{2}\sigma_z} = i\sigma_y + \varepsilon \cdot i\sigma_x + \mathcal{O}(\varepsilon^2), \quad (\text{A34})$$

where ε is a sufficiently small rotation along σ_z . (The following discussions also apply to other rotation axes than σ_z .) For those regular $\mathbf{k} \notin K^4$ satisfying $B^r(C_4T \cdot \mathbf{k}) = B^r(\mathbf{k}) = i\sigma_y$, the full-rank local Jacobians ensure solutions $\mathbf{p}', \mathbf{p} \sim \varepsilon$ to $B^r(C_4T \cdot \mathbf{k} + \mathbf{p}') = B^r(\mathbf{k} + \mathbf{p}) = q_{\text{ref}}(\varepsilon)$. Thus, the contribution to $\deg[B^r]$ from $\mathbf{k} \notin K^4$ remains even upon the perturbation, and we only need to examine the contribution from neighborhoods of $\mathbf{k}_0 \in K^4$. Suppose $B^r(\mathbf{k}_0) = i\sigma_y$ ($\mathbf{k}_0 \in K^4$), solutions to the equation $B^r(\mathbf{k}_0 + \mathbf{p}) = q_{\text{ref}}(\varepsilon)$, *i.e.*,

$$\beta_{01}p_z + \beta_{02}(p_x^2 - p_y^2) + 2\beta_{03}p_xp_y = \mathcal{O}(\varepsilon^2), \quad (\text{A35})$$

$$\beta_{11}p_z + \beta_{12}(p_x^2 - p_y^2) + 2\beta_{13}p_xp_y = \varepsilon + \mathcal{O}(\varepsilon^2), \quad (\text{A36})$$

$$\beta_{31}p_z + \beta_{32}(p_x^2 - p_y^2) + 2\beta_{33}p_xp_y = \mathcal{O}(\varepsilon^2), \quad (\text{A37})$$

give the split preimages. We expect the solutions to satisfy $|p_z| \sim \varepsilon$, $|p_{x,y}| \sim \varepsilon^{\frac{1}{2}}$. Eqs. (A35) and (A37) imply

$$(p_x^2 - p_y^2) \cdot \sin 2\varphi + 2p_xp_y \cdot \cos 2\varphi = \mathcal{O}(\varepsilon^2), \quad (\text{A38})$$

where $2\varphi = \arctan \frac{\beta_{02}\beta_{31} - \beta_{32}\beta_{01}}{\beta_{03}\beta_{31} - \beta_{33}\beta_{01}} \in (-\frac{\pi}{2}, \frac{\pi}{2}]$. We introduce a coordinate transformation $p_x = p_1 \cdot \cos \varphi + p_2 \cdot \sin \varphi$, $p_y = -p_1 \cdot \sin \varphi + p_2 \cdot \cos \varphi$ such that $p_x^2 - p_y^2 = (p_1^2 - p_2^2) \cdot \cos 2\varphi + 2p_1p_2 \cdot \sin 2\varphi$, $2p_xp_y = -(p_1^2 - p_2^2) \cdot \sin 2\varphi + 2p_1p_2 \cdot \cos 2\varphi$. Then the above equation becomes

$$p_1p_2 = 0 + \mathcal{O}(\varepsilon^2). \quad (\text{A39})$$

Using the new coordinates, we find two branches of solutions to Eqs. (A35) and (A37):

$$\text{Curve-I: } p_1 = 0 + \mathcal{O}(\varepsilon^{\frac{3}{2}}), \quad p_z = p_2^2 \cdot \frac{\cos 2\varphi \cdot \beta_{02} - \sin 2\varphi \cdot \beta_{03}}{\beta_{01}} + \mathcal{O}(\varepsilon^2), \quad (\text{A40})$$

$$\text{Curve-II: } p_2 = 0 + \mathcal{O}(\varepsilon^{\frac{3}{2}}), \quad p_z = -p_1^2 \cdot \frac{\cos 2\varphi \cdot \beta_{02} - \sin 2\varphi \cdot \beta_{03}}{\beta_{01}} + \mathcal{O}(\varepsilon^2). \quad (\text{A41})$$

The remaining Eq. (A36) gives a curve in the $p_1 = 0$ plane

$$p_1 = 0 + \mathcal{O}(\varepsilon^{\frac{3}{2}}), \quad p_z = \frac{\varepsilon}{\beta_{11}} + p_2^2 \frac{\cos 2\varphi \cdot \beta_{12} - \sin 2\varphi \cdot \beta_{13}}{\beta_{11}} + \mathcal{O}(\varepsilon^2), \quad (\text{A42})$$

which may have two or zero crossings with curve-I. Eq. (A36) also gives another curve in the $p_2 = 0$ plane

$$p_2 = 0 + \mathcal{O}(\varepsilon^{\frac{3}{2}}), \quad p_z = \frac{\varepsilon}{\beta_{11}} - p_1^2 \frac{\cos 2\varphi \cdot \beta_{12} - \sin 2\varphi \cdot \beta_{13}}{\beta_{11}} + \mathcal{O}(\varepsilon^2), \quad (\text{A43})$$

which may have zero or two crossings with curve-II. Thus, the number of solutions to Eqs. (A35) to (A37) is even, and they are regular points because in general the Jacobian determinant (Eq. (A33)) is proportional to $p_x^2 + p_y^2 \sim |\varepsilon| > 0$. Therefore, a critical point $\mathbf{k}_0 \in K^4$ splits into an even number of regular points upon the perturbation Eq. (A34), contributing trivially to $\deg[B^r] \bmod 2$ (Eq. (A28)).

The proof for $P_3 = 0 \bmod 1$ is completed.

3. Complexity from C_2 sewing matrix

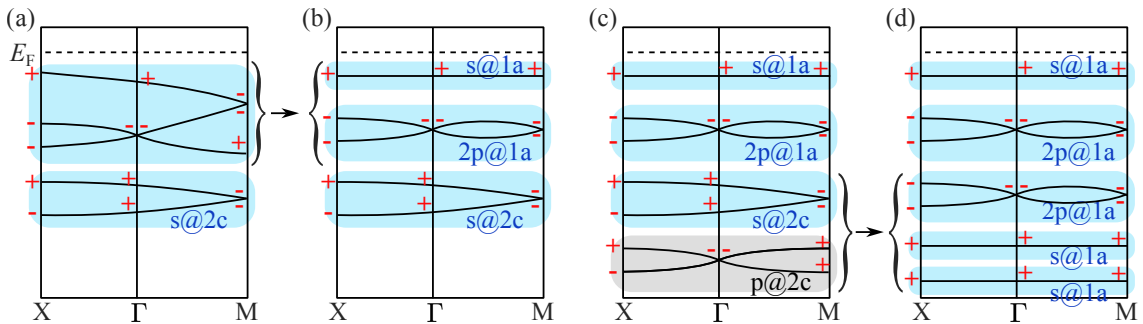


FIG. 4. Adiabatic deformation of the occupied bands. The red \pm signs indicate the C_2 eigenvalues. Bands shaded in blue form C_2 -BRs, which are BRs of the space group $P2$ but may exhibit stable topology protected by C_4T in principle. Bands shaded in grey form C_4T -BRs, which are in trivial atomic limits. (a) and (b) demonstrate how the occupied bands are deformed into disconnected 1D and 2D blocks. (c) and (d) demonstrate how a generic C_2 -BR is deformed into a C_2 -BR induced from the $1a$ position by adding auxiliary C_4T -BRs.

Let us enumerate the elementary BRs - minimal symmetry-allowed atomic limits - of space group $P2$ and derive their C_2 sewing matrices D^r . There are four C_2 invariant Wyckoff positions in real space: $(0, 0, z)$, $(\frac{1}{2}, \frac{1}{2}, z)$, $(\frac{1}{2}, 0, z)$, $(0, \frac{1}{2}, z)$, where

z is a free parameter ranging from 0 to 1. Without loss of generality, in the following we choose $z = 0$. We use $|\mathbf{R} + \mathbf{t}, \xi\rangle$ to represent a local orbital locating at $\mathbf{R} + \mathbf{t}$ with C_2 eigenvalue $\xi = \pm 1$. Here \mathbf{R} represents the unit cell and \mathbf{t} is the corresponding Wyckoff position. C_2 acts on the local orbital as $C_2|\mathbf{R} + \mathbf{t}, \xi\rangle = \xi|-\mathbf{R} - \mathbf{t}, \xi\rangle$. The Bloch states are Fourier transformations

$$|\psi_\xi(\mathbf{k})\rangle = \frac{1}{\sqrt{N}} \sum_{\mathbf{R}} e^{i\mathbf{R}\cdot\mathbf{k}} |\mathbf{R} + \mathbf{t}, \xi\rangle, \quad (\text{A44})$$

where N is the system size. They are periodic over the Brillouin zone. One can directly verify that

$$C_2|\psi_\xi(\mathbf{k})\rangle = \xi \frac{1}{\sqrt{N}} \sum_{\mathbf{R}} e^{i\mathbf{R}\cdot\mathbf{k}} |-\mathbf{R} - \mathbf{t}, \xi\rangle = \xi \frac{1}{\sqrt{N}} \sum_{\mathbf{R}'} e^{i(-\mathbf{R}' - 2\mathbf{t})\cdot\mathbf{k}} |\mathbf{R}' + \mathbf{t}, \xi\rangle = \xi e^{-i2\mathbf{t}\cdot\mathbf{k}} |\psi_\xi(C_2\mathbf{k})\rangle, \quad (\text{A45})$$

where $\mathbf{R}' = -\mathbf{R} - 2\mathbf{t}$. We can read the C_2 sewing matrix as

$$D_{\mathbf{t},\xi}(\mathbf{k}) = \xi e^{-i2\mathbf{t}\cdot\mathbf{k}}. \quad (\text{A46})$$

For later convenience, we introduce Wyckoff position labels for the magnetic space group $P4'$:

$$1a : (0, 0, 0), \quad 1b : \left(\frac{1}{2}, \frac{1}{2}, 0\right), \quad 2c : \left(\frac{1}{2}, 0, 0\right), \left(0, \frac{1}{2}, 0\right), \quad (\text{A47})$$

where $1a$ and $1b$ is C_4T symmetric, and the two positions in $2c$ transform to each under C_4T .

As explained in the last subsection, since C_2 does not protect any stable topology, the nine C_2 sewing matrices in Eqs. (A22) to (A24) should be identical to that of BRs or fragile topological bands of the space group $P2$. We hence refer to them as C_2 -BRs (or C_2 -fragile-bands). It might be worth emphasizing that such C_2 -BRs are C_4T -symmetric, and the C_4T sewing matrix $B^r(\mathbf{k})$ could be atomic or topological. For clarity, in the following we refer to the trivial atomic limits respecting the C_4T symmetry as C_4T -BRs, whose $B^r(\mathbf{k})$ matrix is atomic. A C_4T -BR is by definition a C_2 -BR, but the reverse is not necessarily true. We observe that four of the C_2 sewing matrices in Eqs. (A22) to (A24) (marked red) are consistent with C_2 -BRs. The first (dubbed as $2p@1b$) can be obtained from two $\xi = -1$ states at $1b$. The corresponding sewing matrix is

$$D^r(\mathbf{k}) = -\sigma_0 \cdot e^{-i(k_x+k_y)}, \quad (2p@1b). \quad (\text{A48})$$

The second (dubbed as $2p@1a$) can be obtained from two $\xi = -1$ states at $1a$. The corresponding sewing matrix is

$$D^r(\mathbf{k}) = -\sigma_0, \quad (2p@1a). \quad (\text{A49})$$

The third (dubbed as $p@2c$) can be obtained from two $\xi = -1$ states at $2c$, respectively. The corresponding sewing matrix is

$$D^r(\mathbf{k}) = \begin{pmatrix} -e^{-ik_x} & 0 \\ 0 & -e^{-ik_y} \end{pmatrix}, \quad (p@2c). \quad (\text{A50})$$

The fourth (dubbed as $s@2c$) can be obtained from two $\xi = 1$ states at $2c$, respectively. The corresponding sewing matrix is

$$D^r(\mathbf{k}) = \begin{pmatrix} e^{-ik_x} & 0 \\ 0 & e^{-ik_y} \end{pmatrix}, \quad (s@2c). \quad (\text{A51})$$

One can similarly derive the two 1D C_2 -BRs

$$D^r(\mathbf{k}) = 1, \quad (s@1a), \quad (\text{A52})$$

$$D^r(\mathbf{k}) = e^{-i(k_x+k_y)}, \quad (s@1b). \quad (\text{A53})$$

The other five sewing matrices (not marked red) in Eqs. (A22) to (A24) must represent C_2 -fragile-bands.

In the last subsection, we have deformed the occupied bands into disconnected blocks where any possible accidental degeneracy is lifted by perturbation terms that do not change the topology. Then we proved that a block does not contribute to P_3 if it is a C_2 -BR ($s@1a$ or $2p@1a$) induced from the $1a$ position, whose C_2 sewing matrix is a constant (Eq. (A25)). Here we show that other C_2 -BRs cannot contribute to P_3 neither. First, as long as the occupied bands as a whole do not exhibit fragile topology, we can always deform them into disconnected blocks where each is a C_2 -BR. Even the occupied bands exhibit a fragile topology as a whole, we can always add auxiliary atomic limits into the occupied bands - without changing the stable topology characterized by P_3 - to trivialize the fragile topology. This is because the defining feature of fragile topology is that it can be trivialized by adding atomic limits, which, as completely localized states, do not contribute to P_3 . Therefore, in order to calculate P_3 , we can always safely assume that the occupied bands can be deformed into disconnected C_2 -BRs.

Second, using the same trick of adding auxiliary atomic BRs, we can always deform the occupied bands into a set of 1D and 2D C_2 -BRs induced from the $1a$ position. Now we explicitly construct the adiabatic deformations for the C_2 -BRs $s@2c$, $p@2c$, $2p@1b$, $s@1b$.

- (i) For a 2D block forming a C_2 -BR $s@2c$, whose C_4T sewing matrix $B^r(\mathbf{k})$ may or may not characterize a stable topology, we couple it to an auxiliary C_4T -BR $p@2c$, whose $B^r(\mathbf{k})$ matrix is atomic, such that the four bands $[s@2c] \oplus [p@2c]$ are equivalent to a C_2 -BR $[s@1a] \oplus [s@1a] \oplus [2p@1a]$. To be specific, we write the C_2 sewing matrix of $[s@2c] \oplus [p@2c]$ as

$$D(\mathbf{k}) = \text{diag} \left(e^{-ik_x} \quad e^{-ik_y} \quad -e^{-ik_x} \quad -e^{-ik_y} \right) \quad (\text{A54})$$

Notice that a gauge transformation to the Bloch state basis $|\psi'_n(\mathbf{k})\rangle = |\psi_m(\mathbf{k})\rangle U_{mn}(\mathbf{k})$ changes the C_2 sewing matrix to $D'(\mathbf{k}) = U^\dagger(C_2 \mathbf{k}) \cdot D(\mathbf{k}) \cdot U(\mathbf{k})$. We find the gauge transformation

$$U(\mathbf{k}) = \begin{pmatrix} \frac{1+e^{ik_x}}{2} & 0 & \frac{1-e^{ik_x}}{2} & 0 \\ 0 & \frac{1+e^{ik_y}}{2} & 0 & \frac{1-e^{ik_y}}{2} \\ \frac{1-e^{ik_x}}{2} & 0 & \frac{1+e^{ik_x}}{2} & 0 \\ 0 & \frac{1+e^{ik_y}}{2} & 0 & \frac{1-e^{ik_y}}{2} \end{pmatrix} \quad (\text{A55})$$

changes the C_2 sewing matrix to that of a C_2 -BR $[s@1a] \oplus [s@1a] \oplus [2p@1a]$:

$$D'(\mathbf{k}) = U^\dagger(C_2 \cdot \mathbf{k}) \cdot D(\mathbf{k}) \cdot U(\mathbf{k}) = \text{diag} (1 \quad 1 \quad -1 \quad -1) . \quad (\text{A56})$$

Thus, the adiabatic deformation shown in Fig. 4(c) and (d) can be realized by the Hamiltonian

$$(1 - \delta) \cdot \sum_{\mathbf{k}} \sum_{n,m=1}^4 h_{nm}(\mathbf{k}) |\psi_n(\mathbf{k})\rangle \langle \psi_m(\mathbf{k})| + \delta \cdot \sum_{\mathbf{k}} \sum_{n,m=1}^4 h'_{nm}(\mathbf{k}) |\psi'_n(\mathbf{k})\rangle \langle \psi'_m(\mathbf{k})| , \quad (\text{A57})$$

where $h(\mathbf{k})$ and $h'(\mathbf{k})$ give the bands shown in Fig. 4(c) and (d), respectively, and δ is continuously turned from 0 to 1.

- (ii) For a 2D block forming a C_2 -BR $p@2c$, we can add an auxiliary C_4T -BR $s@2c$ and apply the same U (Eq. (A55)) to transform them to a C_2 -BR $[s@1a] \oplus [s@1a] \oplus [2p@1a]$. Then an adiabatic deformation similar to Eq. (A57) can be introduced.
- (iii) For a 2D block forming a C_2 -BR $2p@1b$, we can add an auxiliary C_4T -BR $[s@1b] \oplus [s@1b]$ and transform them to a C_2 -BR $[2p@1a] \oplus [s@1a] \oplus [s@1a]$. To be specific, we write the C_2 sewing matrix of $[2p@1b] \oplus [s@1b] \oplus [s@1b]$ as

$$D(\mathbf{k}) = \text{diag} \left(-e^{-i(k_x+k_y)} \quad -e^{-i(k_x+k_y)} \quad e^{-i(k_x+k_y)} \quad e^{-i(k_x+k_y)} \right) . \quad (\text{A58})$$

We find the gauge transformation

$$U(\mathbf{k}) = \begin{pmatrix} \frac{1+e^{i(k_x+k_y)}}{2} & 0 & \frac{1-e^{i(k_x+k_y)}}{2} & 0 \\ 0 & \frac{1+e^{i(k_x+k_y)}}{2} & 0 & \frac{1-e^{i(k_x+k_y)}}{2} \\ \frac{1-e^{i(k_x+k_y)}}{2} & 0 & \frac{1+e^{i(k_x+k_y)}}{2} & 0 \\ 0 & \frac{1+e^{i(k_x+k_y)}}{2} & 0 & \frac{1-e^{i(k_x+k_y)}}{2} \end{pmatrix} \quad (\text{A59})$$

changes the C_2 sewing matrix to that of a C_2 -BR $[2p@1a] \oplus [s@1a] \oplus [s@1a]$:

$$D'(\mathbf{k}) = U^\dagger(C_2 \cdot \mathbf{k}) \cdot D(\mathbf{k}) \cdot U(\mathbf{k}) = \text{diag} (-1 \quad -1 \quad 1 \quad 1) . \quad (\text{A60})$$

An adiabatic deformation similar to Eq. (A57) can be introduced then.

- (iv) For a 1D block forming a C_2 -BR $s@1b$, we can add an auxiliary C_4T -BR $[s@1b] \oplus [2p@1b]$ and apply the same U (Eq. (A59)) to transform into a C_2 -BR $[2p@1a] \oplus [s@1a] \oplus [s@1a]$. Then an adiabatic deformation similar to Eq. (A57) can be introduced.

Therefore, in terms of the C_2 sewing matrix, the occupied bands can always be deformed into a set of C_2 -BRs induced from the 1a position, whose C_2 sewing matrices are \mathbf{k} -independent (Eq. (A25)).

B. Topological crystal

In this section, we argue that the single-valued magnetic space group $P4'$, where $(C_4T)^4 = 1$, protects no clean topological crystalline insulator (TCI) states following the topological crystal method.

Let us first introduce the real space cell decomposition for $P4'$. Following Ref. [24], an asymmetric unit (AU) is defined as a largest connected open region in three dimensional space that has no overlap with its symmetry partners. The choice of AU is not unique, but we can always choose it as a convex polyhedron. The AU is then copied throughout space using crystalline symmetry operations, and the resulting nonoverlapping union of the copies is denoted \mathcal{A} . The complement of the open set \mathcal{A} in three dimensional space is a two-skeleton denoted X^2 . A 3-cell is one of the copies of AU in \mathcal{A} . A 2-cell is an oriented open segment of a plane separating two 3-cells, which does not overlap with its symmetry partners. Similarly, 1-cells are oriented open segments of lines between different 2-cells that does not overlap with its symmetry partners, and 0-cells are points joining different 1-cells. The construction of n -cells ($0 \leq n \leq 3$) gives the three dimensional space a cell complex structure. A unit cell with C_4T symmetry is shown in Fig. 5(a). For simplicity, we define the positive orientation of each 2-cell and 1-cell to be either $+x$, $+y$ or $+z$. The red and blue lines α, β are the two C_4T centers in the unit cell. The three basis lattice vectors are $\mathbf{a}_1, \mathbf{a}_2, \mathbf{a}_3$ respectively. Fig. 5(b-e) show the cell decomposition of the unit cell. There are four 3-cells, twelve 2-cells, twelve 1-cells, and four 0-cells in each unit cell, which are labeled by $a_i, b_j, c_k, d_l, 1 \leq i, l \leq 4, 1 \leq j, k \leq 12$ respectively. There are also n -cells in the figure that belong to other unit cells, and are thus lattice translations of the labeled n -cells mentioned above. We assume translational symmetry in this section, and treat these n -cells in the same way as their translation partners. For example, the 1-cell shown by the dashed blue line in the second row of Fig. 5(d) is also labeled c_1 since it can be obtained from the 1-cell c_1 in the unit cell (the solid blue line) by a lattice translation \mathbf{a}_1 .

Now let us consider how the n -cells are transformed to each other by crystalline symmetries. Apparently, the C_4T operation transforms $a_1 \rightarrow a_2 \rightarrow a_3 \rightarrow a_4 \rightarrow a_1$ (Fig. 5(b)), so all 3-cells in the lattice are symmetry equivalent. For the 2-cells (Fig. 5(c)), C_4T operation transforms $b_1 \rightarrow b_2 \rightarrow -b_3 \rightarrow -b_4 \rightarrow b_1, b_5 \rightarrow -b_7 \rightarrow -b_6 \rightarrow b_8 \rightarrow b_5$, and $b_9 \rightarrow b_{10} \rightarrow b_{11} \rightarrow b_{12} \rightarrow b_9$. It is apparent that neither C_4T nor lattice translation can transform the above three cycles to each other, so there are three distinct symmetry equivalent classes of 2-cells: $b_{1,2,3,4}, b_{5,6,7,8}$, and $b_{9,10,11,12}$. Now let us consider the 1-cells (Fig. 5(d)). c_1 and c_4 lie on the two C_4T axes α, β respectively. The relative position between them is $\frac{1}{2}(\mathbf{a}_1 + \mathbf{a}_2)$, which is not a lattice vector. It is also apparent that they cannot be transformed to each other by the C_4T operation. They are also not symmetry equivalent to the other 1-cells since they lie on the only two C_4T axes, so each of them forms a symmetry equivalent class by itself. The two other 1-cells parallel to z direction are c_2 and c_3 . C_4T operation transforms $c_3 \rightarrow c_2$. Since they are obviously not symmetry equivalent to the 1-cells parallel to the xy plane, $c_{2,3}$ form a symmetry equivalent class. Among the 1-cells parallel to the xy plane, C_4T operation transforms $c_5 \rightarrow c_{11} \rightarrow -c_6 \rightarrow -c_{12} \rightarrow c_5$, and $c_9 \rightarrow -c_8 \rightarrow -c_{10} \rightarrow c_7 \rightarrow c_9$, but cannot relate the above two cycles. Therefore, $c_{5,6,11,12}$ and $c_{7,8,9,10}$ form two distinct symmetry equivalent classes of 1-cells. In summary, the twelve 1-cells can be divided into five different symmetry equivalent classes: $c_1, c_4, c_{2,3}, c_{5,6,11,12}$ and $c_{7,8,9,10}$. The four 0-cells $d_{1,2,3,4}$ (Fig. 5(e)) are ends of the four 1-cells that are parallel to z direction $c_{1,2,3,4}$ respectively, so following above discussions, they can be divided into three different symmetry equivalent classes: $d_1, d_4, d_{2,3}$. In summary, there are 1, 3, 5, 3 distinct symmetry equivalent classes of 3, 2, 1, 0-cells respectively. In Fig. 5(c-e), symmetry equivalent n -cells are shown in the same color to emphasize their relationships.

Following Refs. [21, 22, 24], a topological crystal is defined as a gapped decoration of lower-dimensional TIs on the n -cells ($n \leq 2$) that respects the crystalline symmetry. Now let us repeat the argument that a TCI state can always be adiabatically connected to a topological crystal. Since there is no 3D strong TIs protected by local symmetry in the considered symmetry class A, one can always trivialize the AU by deforming it into a set of occupied local orbitals. This is always accessible provided $\xi \ll a_{AU}$, where ξ is the characteristic correlation length of the TCI ground state, and a_{AU} is the linear size of the AU. Since TCI ground states are short range correlated, it is reasonable to expect that by adding a fine enough mesh of trivial degrees of freedom in the AU, ξ can be made as small as required, while a_{AU} remains unchanged. $\xi \ll a_{AU}$ is thus satisfied, and the desired adiabatic path can be found. The adiabatic path is then copied throughout space using crystalline symmetry to trivialize the open set \mathcal{A} . It is obvious that such a copy always respects the crystalline symmetry. After the above adiabatic deformation, the topologically nontrivial elements can only lie on the two-skeleton X^2 , and can be decomposed to lower-dimensional TIs decorated on n -cells, $n \leq 2$. Ref. [24] shows that a full classification of all TCIs with spin-orbit coupling and time reversal symmetry can be obtained by topological crystals, proving the validity of the above argument. Since symmetry class A has no 0- and 1-dimensional TIs, we only consider decorations of Chern insulators on the 2-cells.

In a cell complex structure, the boundary of an n -cell can be expanded in terms of oriented $(n-1)$ -cells. For examples: $\partial a_1 = b_7 + b_2 - b_1 - b_6$ for 3-cells, $\partial b_1 = -c_2 + c_4, \partial b_5 = c_1 - c_2$, and $\partial b_9 = c_6 + c_{11} - c_8 - c_9$ for 2-cells, $\partial c_1 = d_1 - d_1 = 0, \partial c_2 = 0, \partial c_4 = 0, \partial c_5 = -d_1 + d_2$, and $\partial c_7 = -d_3 + d_4$ for 1-cells. Such boundary mappings will be used for the gluing conditions and bubble equivalence of the topological crystal.

Concerning decorations of Chern insulators on 2-cells, the gluing condition requires an equal number of chiral modes propagating in opposite directions on each 1-cell so that it is possible for them to be locally gapped. Here we show that such conditions, together with the crystalline symmetry, make restrictions on possible decorations. A decoration of Chern insulators on 2-cells in Fig. 5(c) is described by twelve integers $C_{b_j} \in \mathbb{Z}, 1 \leq j \leq 12$, which are the Chern numbers of decorated

Chern insulators on the 2-cells b_j , with the same orientation as discussed above. Using the crystalline symmetry and the fact that time reversal operation reverses the Chern number, the description can be simplified to three integers $C_1, C_2, C_3 \in \mathbb{Z}$: $C_{b_1} = -C_{b_2} = -C_{b_3} = C_{b_4} = C_1$, $C_{b_5} = C_{b_7} = -C_{b_6} = -C_{b_8} = C_2$, and $C_{b_9} = -C_{b_{10}} = C_{b_{11}} = -C_{b_{12}} = C_3$. Since there are five different symmetry equivalent classes of 1-cells, there are also five symmetry inequivalent gluing conditions (for c_1, c_2, c_4, c_5, c_7 respectively):

$$\begin{aligned}
C_{b_5} - C_{b_7} - C_{b_6} + C_{b_8} &= 0 \\
-C_{b_1} + C_{b_3} + C_{b_6} - C_{b_5} &= 0 \\
C_{b_1} + C_{b_2} - C_{b_3} - C_{b_4} &= 0 \\
C_{b_{12}} - C_{b_{11}} &= 0 \\
-C_{b_{12}} + C_{b_{11}} &= 0
\end{aligned} \tag{B1}$$

where we have used translational symmetry implicitly. The first and third rows are automatically satisfied, the second row requires $C_1 = -C_2$, and the last two rows require $C_3 = 0$. We hence conclude that decorations of Chern insulators with $C_{b_1} = -C_{b_2} = -C_{b_3} = C_{b_4} = -C_{b_5} = C_{b_8} = C_{b_6} = -C_{b_7} = C \in \mathbb{Z}$, $C_{b_9} = C_{b_{10}} = C_{b_{11}} = C_{b_{12}} = 0$ are the only possible decorations that satisfy both the crystalline symmetry and gluing conditions.

Since Chern insulators have a \mathbb{Z} classification, one can make a decoration with C any nonzero integer. However, here we show that some of the decorations can be adiabatically connected to the trivial $C = 0$ case by creating Chern bubbles from vacuum and locally annihilating Chern insulators with opposite Chern numbers, a process called ‘‘bubble equivalence’’ in Ref. [24]. Create a bubble of a $C = -1$ state within the AU as well as its symmetry partners, as shown in Fig. 5(f). Expand these bubbles until they are touching the 2-cells, the resulted decoration is given by

$$-\partial a_1 + \partial a_2 - \partial a_3 + \partial a_4 = 2b_1 - 2b_2 - 2b_3 + 2b_4 - 2b_5 - 2b_7 + 2b_6 + 2b_8. \tag{B2}$$

Here the integer coefficients of the 2-cells represent the corresponding Chern numbers. The above equation gives a $C = 2$ decoration. Creating bubbles with other Chern numbers yield all $C \in \text{even}$ decorations. Therefore, after modulo the bubble equivalence, we obtain a \mathbb{Z}_2 classification represented by the $C = 0, 1$ decorations.

Now we show that the $C = 1$ decoration is equivalent to the decoration in Fig.1(c) in the main text. Unlike c_1, c_4 , the four chiral modes on c_2, c_3 have only C_2 symmetry, and can be paired and gapped. Consider the dimerization shown in Fig. 5(g), which effectively joins Chern insulators decorated on b_5 with b_1, b_3 with b_6, b_4 with b_8 , and b_2 with b_7 . After a deformation respecting C_4T symmetry, we arrive at the same decoration as shown in Fig.1(c) of the main text, whose low energy physics is realized by the lattice model.

The above discussion seems apply to both $(C_4T)^4 = 1$ and -1 cases. However, when $(C_4T)^4 = 1$, the $C = 1$ decoration must be gapless according to the discussion in the main text. Therefore, no gapped topological state can be constructed in the framework of topological crystal, suggesting a trivial classification in the clean limit.

We now show that the $C = 1$ decoration can be gapped if $(C_4T)^4 = -1$. Consider four chiral modes 1, 2, 3, 4 on a hinge, which are transformed as $1 \rightarrow 2 \rightarrow 3 \rightarrow 4 \rightarrow 1$ by the C_4T operation, and are propagating in $+z, -z, +z, -z$ direction respectively with velocity v . Let us span the four-by-four Hilbert space with two sets of Pauli matrices $\sigma_{0,x,y,z}, \tau_{0,x,y,z}$, where $\{\tau_z, \sigma_z\} = \{+, +\}, \{+, -\}, \{-, +\}, \{-, -\}$ denote chiral mode 1, 2, 3, 4 respectively. The four-by-four Hamiltonian of the four modes is

$$H(k_z) = vk_z \tau_0 \sigma_z \tag{B3}$$

Consider the $(C_4T)^4 = -1$ symmetry $C_4T = D(C_4T)K$, where K is the complex conjugation, and

$$D(C_4T) = \begin{pmatrix} 0 & 0 & 0 & 1 \\ i & 0 & 0 & 0 \\ 0 & -1 & 0 & 0 \\ 0 & 0 & -i & 0 \end{pmatrix}, \quad D(C_4T)D^*(C_4T)D(C_4T)D^*(C_4T) = -1 \tag{B4}$$

Since $D(C_4T)H^*(k_z)D^\dagger(C_4T) = H(-k_z)$, $D(C_4T)(\tau_x \sigma_x)^*D^\dagger(C_4T) = \tau_0 \sigma_y$, and $D(C_4T)(\tau_0 \sigma_y)^*D^\dagger(C_4T) = \tau_x \sigma_x$, a mass term $m(\tau_x \sigma_x + \tau_0 \sigma_y)$ can be added to $H(k_z)$ without breaking the $(C_4T)^4 = -1$ symmetry. Since $\tau_0 \sigma_z, \tau_x \sigma_x$ and $\tau_0 \sigma_y$ anti-commute with one another, the two pairs of energy bands are $E_\pm(k_z) = \pm \sqrt{(vk_z)^2 + 2m^2}$. This allows the construction of a topological crystal for a clean axion insulator if $(C_4T)^4 = -1$, consistent with the previous discussions in Refs. [45, 50].

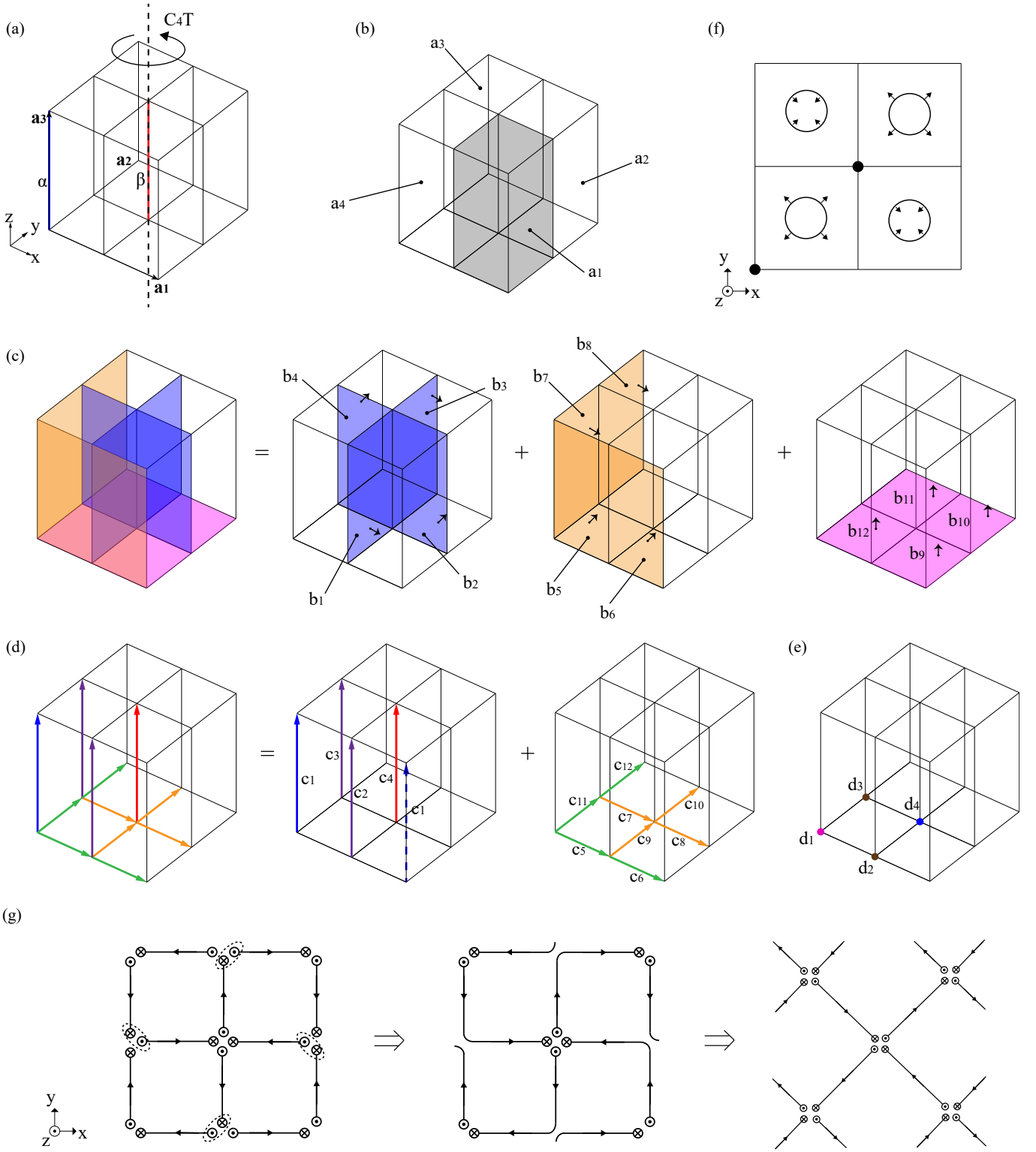


FIG. 5. (a) A unit cell of the cell-complex structure with magnetic space group $P4'$. $\mathbf{a}_1, \mathbf{a}_2, \mathbf{a}_3$ are the three basis vectors. α, β are the two C_4T axes in the unit cell. In the paragraph, “ C_4T operation” refers to the one shown by the arrow unless otherwise specified. (b) The four 3-cells in the unit cell. The 3-cell a_1 is shown in grey, $a_{2,3,4}$ are transformed from a_1 by C_4T around β axis. (c) The twelve 2-cells in the unit cell. (d) The twelve 1-cells in the unit cell. The dashed blue line is the \mathbf{a}_1 translation of the solid blue line, so both are labeled c_1 . The positive orientation of 2-cells and 1-cells are either $+x, +y$ or $+z$, as shown by the arrows in (c) and (d). (e) The four 0-cells in the unit cell. The n -cells in (c-e) with same color are equivalent up to crystalline symmetry operations. (f) (upper right) By creating a Chern bubble (the oriented circle) with $C = -1$ in the AU (3-cell a_1) and its symmetry partners and expanding the Chern bubbles to the boundaries of 3-cells, we arrive at the decoration with $C = 2$, demonstrating the “bubble equivalence” of $C \in \text{even}$ to $C = 0$. (g) The $C = 1$ decoration is equivalent to Fig.1(c) in the main text up to gapping paired chiral edges and a spatial deformation.

C. The lattice model

1. Model and symmetry

Here we give a complete description of the lattice model given in Eq. (2) in the main text. As shown in Fig. 6(a), a unit cell has 8 orbitals. We use three sets of Pauli matrices $\rho_{0,x,y,z}, \tau_{0,x,y,z}, \sigma_{0,x,y,z}$ to span the eight-by-eight Hilbert space. $\rho_z = 1, -1$ correspond to the two squares in a unit cell, $\tau_z = 1, -1$ further labels the two columns in each square, and $\sigma_z = 1, -1$ labels the two sites within each column. The Hamiltonian in momentum space takes the form

$$\begin{aligned} H(\mathbf{k}) = & (m + 2t - 2t \cos k_z) \rho_x \tau_x \sigma_x + 2t \sin k_z \rho_z \tau_z \sigma_z \\ & + \gamma \left(\cos \frac{k_x}{2} \rho_0 \tau_x \sigma_0 - \sin \frac{k_x}{2} \rho_0 \tau_y \sigma_0 + \cos \frac{k_y}{2} \rho_0 \tau_0 \sigma_x - \sin \frac{k_y}{2} \rho_0 \tau_0 \sigma_y \right) \\ & + \lambda \left(\cos \frac{k_x}{2} \cos \frac{k_y}{2} \rho_0 \tau_x \sigma_x + \sin \frac{k_x}{2} \sin \frac{k_y}{2} \rho_0 \tau_y \sigma_y - \sin \frac{k_x}{2} \cos \frac{k_y}{2} \rho_0 \tau_y \sigma_x - \cos \frac{k_x}{2} \sin \frac{k_y}{2} \rho_0 \tau_x \sigma_y \right) \end{aligned} \quad (\text{C1})$$

The first row of Eq. (C1) defines four pairs of chiral and anti-chiral states in the z -direction. For example, the 1st and 8th orbitals span the Hamiltonian $(m + 2t - 2t \cos k_z) \sigma_x + 2t \sin k_z \sigma_z$, where $\sigma_z = 1, -1$ correspond to 1st and 8th orbitals, respectively. When m is small, it reduces to a Dirac Hamiltonian around $k_z = 0$: $(m + tk_z^2) \sigma_x + 2tk_z \sigma_z + \mathcal{O}(k_z^3)$, and has a large gap around $k_z = \pi$. Thus, the 1st and 8th orbitals simulate a pair of anti-chiral and chiral edge modes of a Chern block shown in Fig. 1(c) of the main text. m is the coupling between two edges, and it should approach zero if the Chern block is sufficiently large. In this work we use m as a tuning parameter. Similarly, 2nd and 7th orbitals, 3rd and 6th orbitals, 4th and 5th orbitals form the other three pairs of anti-chiral and chiral states, respectively. γ in the second row of Eq. (C1) is the hopping between nearest neighbors within each square. λ in the third row of Eq. (C1) is the hopping along the diagonals of each square.

We have adopt a symmetric gauge for Eq. (C1). In this gauge, the eight Bloch bases are defined as

$$|\phi_{\alpha, \mathbf{k}}\rangle = \frac{1}{\sqrt{N}} \sum_{\mathbf{R}} e^{i\mathbf{k} \cdot (\mathbf{R} + \mathbf{t}_\alpha)} |\mathbf{R}, \alpha\rangle \quad (\text{C2})$$

where $|\mathbf{R}\alpha\rangle$ ($\alpha = 1 \cdots 8$) is a local orbital locating at $\mathbf{R} + \mathbf{t}_\alpha$, N is the number of unit cells, \mathbf{R} sums over lattice vector, and \mathbf{t}_α is the sublattice vector for the α -th orbital. We choose

$$\begin{aligned} \mathbf{t}_1 = & (\delta, \delta, 0), \quad \mathbf{t}_2 = \left(\delta, \frac{1}{2} - \delta, 0\right), \quad \mathbf{t}_3 = \left(\frac{1}{2} - \delta, \delta, 0\right), \quad \mathbf{t}_4 = \left(\frac{1}{2} - \delta, \frac{1}{2} - \delta, 0\right), \\ \mathbf{t}_5 = & \left(\frac{1}{2} + \delta, \frac{1}{2} + \delta, 0\right), \quad \mathbf{t}_6 = \left(\frac{1}{2} + \delta, -\delta, 0\right), \quad \mathbf{t}_7 = \left(-\delta, \frac{1}{2} + \delta, 0\right), \quad \mathbf{t}_8 = (-\delta, -\delta, 0), \end{aligned} \quad (\text{C3})$$

where $\delta > 0$ is a small quantity. In Fig. 6 we use a finite δ for illustration. But in practical calculation we take the $\delta \rightarrow 0$ limit for simplicity. $H(\mathbf{k})$ is the Hamiltonian matrix on the Bloch basis, *i.e.*, $H_{\alpha\beta}(\mathbf{k}) = \langle \phi_{\alpha, \mathbf{k}} | \hat{H} | \phi_{\beta, \mathbf{k}} \rangle$. The $\cos \frac{k_x, y}{2}$ and $\sin \frac{k_x, y}{2}$ factors in Eq. (C1) come from phase factors $e^{i\mathbf{k} \cdot (\mathbf{t}_\alpha - \mathbf{t}_\beta)}$ appearing along hoppings between the α -th and β -th orbitals. The Bloch basis satisfies a twisted boundary condition over the Brillouin zone

$$|\phi_{\alpha, \mathbf{k} + \mathbf{G}}\rangle = |\phi_{\beta, \mathbf{k}}\rangle V_{\beta\alpha}(\mathbf{G}), \quad V_{\beta\alpha}(\mathbf{G}) = \delta_{\alpha\beta} e^{i\mathbf{G} \cdot \mathbf{t}_\alpha}, \quad (\text{C4})$$

where implicit summation over repeated indices is assumed. It follows that $H(\mathbf{k})$ satisfies

$$H(\mathbf{k} + \mathbf{G}) = V^\dagger(\mathbf{G}) H(\mathbf{k}) V(\mathbf{G}). \quad (\text{C5})$$

$V(\mathbf{G})$ is usually referred to as the embedding matrix.

Now we summarize the symmetries of $H(\mathbf{k})$. First, we show that $H(\mathbf{k})$ breaks the time-reversal symmetry (TRS). As explained in the above two paragraphs, the orbitals $|\mathbf{0}, 1\rangle$ $|\mathbf{0}, 8\rangle$ mimic a pair of anti-chiral and chiral modes at the same position. Thus, TRS, if existed, must interchange $|\mathbf{0}, 1\rangle$ and $|\mathbf{0}, 8\rangle$. For the same reason, TRS must send $|\mathbf{R}, \alpha\rangle$ to $|\mathbf{R}, 9 - \alpha\rangle$. Consider the hopping λ between $|\mathbf{0}, 1\rangle$, $|\mathbf{0}, 2\rangle$, TRS would transform it to a hopping between $|\mathbf{0}, 8\rangle$, $|\mathbf{0}, 7\rangle$, which does not exist in the model (Fig. 6(a)). The model instead has a hopping between $|\mathbf{0}, 7\rangle$ and $|\mathbf{010}, 8\rangle$, wherein the latter is in another unit cell. We find that $H(\mathbf{k})$ enjoys a symmetry group generated by

$$H(\mathbf{k}) = \mathcal{D}(P) \cdot H(-\mathbf{k}) \cdot \mathcal{D}^\dagger(P), \quad \mathcal{D}(P) = \rho_x \tau_x \sigma_x, \quad P = \{-1|\mathbf{0}\}, \quad (\text{C6})$$

$$H(-k_y, k_x, k_z) = \mathcal{D}(\tilde{C}_4) \cdot H(\mathbf{k}) \cdot \mathcal{D}^\dagger(\tilde{C}_4), \quad \mathcal{D}(\tilde{C}_4) = \rho_x \begin{pmatrix} 0 & 0 & 1 & 0 \\ 1 & 0 & 0 & 0 \\ 0 & 0 & 0 & 1 \\ 0 & 1 & 0 & 0 \end{pmatrix}, \quad \tilde{C}_4 = \{4_{001}|0\frac{1}{2}0\}, \quad (\text{C7})$$

$$H(-k_x, k_y, k_z) = \mathcal{D}(\widetilde{M}_x) \cdot H(\mathbf{k}) \cdot \mathcal{D}^\dagger(\widetilde{M}_x), \quad \mathcal{D}(\widetilde{M}_x) = \rho_x \tau_x \sigma_0, \quad \widetilde{M}_x = \{m_{100} | 0 \frac{1}{2} 0\} \quad (\text{C8})$$

$$H(-\mathbf{k}) = \mathcal{D}(\widetilde{T}) \cdot H^*(\mathbf{k}) \cdot \mathcal{D}^\dagger(\widetilde{T}), \quad \mathcal{D}(\widetilde{T}) = \rho_x \tau_0 \sigma_0, \quad \widetilde{T} = \{1' | \frac{1}{2} \frac{1}{2} 0\}. \quad (\text{C9})$$

Here $\{p^{(i)}|\boldsymbol{\tau}\}$ is the Seitz symbol for spatial operations, and a prime in the superscript of p represent a time-reversal operation following the point group operation p . We adopt the convention of the **MGENPOS** program of the Bilbao Crystallographic Server [71, 72]. P is an inversion centered at the origin, \widetilde{C}_4 is a four-fold rotation centered at $(-\frac{1}{4}\frac{1}{4}0)$, \widetilde{M}_x is a glide mirror with respect to the plane $(0, y, z)$, and \widetilde{T} is a magnetic translation. These operations generate the single-valued magnetic space group $P_{C4/nbm}$ (#125.373 in the BNS setting). This group also has $C_4T = \{1|0\bar{1}0\} \cdot \widetilde{T} \cdot \widetilde{C}_4 = \{4'_{001} | \frac{1}{2} 00\}$, $S_4 = P \cdot \widetilde{C}_4^3 = \{-4'_{001} | \frac{1}{2} 00\}$, $M_xT = \{1|0\bar{1}0\} \cdot \widetilde{T} \cdot \widetilde{M}_x = \{m'_{100} | \frac{1}{2} 00\}$, $M_zT = \{1|\bar{1}00\} \cdot \widetilde{T} \cdot P \cdot \widetilde{C}_4^2 = \{m'_{001} | 000\}$, $\widetilde{M}_z = \widetilde{T} \cdot M_zT = \{m_{001} | \frac{1}{2}, \frac{1}{2}, 0\}$ symmetries. Both the C_4T center and the S_4 center locate at $(\frac{1}{4}, \frac{1}{4}, 0)$. The mirror planes of M_xT and M_zT are $(\frac{1}{4}, y, z)$ and $(x, y, 0)$, respectively. \widetilde{M}_z is a glide mirror with respect to the $(x, y, 0)$ plane. For later convenience, we also derive the representation of S_4

$$\mathcal{D}(S_4) = \mathcal{D}(P) \cdot \mathcal{D}^3(\widetilde{C}_4) = \rho_0 \begin{pmatrix} 0 & 0 & 1 & 0 \\ 1 & 0 & 0 & 0 \\ 0 & 0 & 0 & 1 \\ 0 & 1 & 0 & 0 \end{pmatrix}. \quad (\text{C10})$$

Here we also summarize the maximal Wyckoff positions and their magnetic point groups:

$$2a : \quad (\frac{1}{4}, \frac{1}{4}, 0), \quad (\frac{3}{4}, \frac{3}{4}, 0), \quad 4'/m'm'm, \quad 2b : \quad (\frac{1}{4}, \frac{1}{4}, \frac{1}{2}), \quad (\frac{3}{4}, \frac{3}{4}, \frac{1}{2}), \quad 4'/m'm'm, \quad (\text{C11})$$

$$2c : \quad (\frac{1}{4}, \frac{3}{4}, 0), \quad (\frac{3}{4}, \frac{1}{4}, 0), \quad 4/m'm'm', \quad 2d : \quad (\frac{1}{4}, \frac{3}{4}, \frac{1}{2}), \quad (\frac{3}{4}, \frac{1}{4}, \frac{1}{2}), \quad 4/m'm'm', \quad (\text{C12})$$

$$4e : \quad (0, 0, \frac{1}{2}), \quad (\frac{1}{2}, 0, \frac{1}{2}), \quad (0, \frac{1}{2}, \frac{1}{2}), \quad (\frac{1}{2}, \frac{1}{2}, \frac{1}{2}), \quad m'.mm', \quad (\text{C13})$$

$$4f : \quad (0, 0, 0), \quad (\frac{1}{2}, 0, 0), \quad (0, \frac{1}{2}, 0), \quad (\frac{1}{2}, \frac{1}{2}, 0), \quad m'.mm'. \quad (\text{C14})$$

In our convention, the origin is shifted by $(\frac{1}{2}, 0, 0)$ from that on the Bilbao Crystallographic Server.

Let us examine whether Eq. (C1) has a chiral symmetry: $S \cdot H(\mathbf{k}) \cdot S = -H(\mathbf{k})$ with S being a unitary matrix satisfying $S^2 = 1$. For S to anti-commute with the $\rho_0 \tau_0 \sigma_{x,y}$ terms in the second row of Eq. (C1), S must be proportional to σ_z . Similarly, for S to anti-commute with the $\rho_0 \tau_{x,y} \sigma_0$ terms in the second row, S must be proportional to τ_z . Then, S could be a linear combination of $\rho_{0,x,y,z} \tau_z \sigma_z$, all of which commute with the λ terms of Eq. (C1). If $\lambda = 0$, $H(\mathbf{k})$ has an accidental chiral $S = \rho_y \tau_z \sigma_z$. Being off-diagonal in the $\rho_z = \pm 1$ basis, S is *non-local* in real space and hence will be broken by disorder potentials. Therefore, either a finite λ or disorder potential will break the accidental chiral symmetry.

Let us examine whether Eq. (C1) has a particle-hole symmetry: $C \cdot H^*(\mathbf{k}) \cdot C^\dagger = -H(-\mathbf{k})$ with C being a unitary matrix satisfying $C \cdot C^* = \pm 1$. Because of the \widetilde{T} symmetry of $H(\mathbf{k})$ (Eq. (C9)), the existence of C symmetry would automatically imply the presence of a chiral symmetry $S = \rho_x \cdot C$ (up to a $U(1)$ phase factor), and vice versa. According to the discussions in the last paragraph, $H(\mathbf{k})$ would have an accidental $C = \rho_z \tau_z \sigma_z$ when $\lambda = 0$. Either a finite λ or on-site disorder potentials can break this accidental particle-hole symmetry.

In the following, we keep $t = 2, \gamma = 1, \lambda = 0.01$ fixed and discuss how m changes the band structure of the system. For convenience, we define the high symmetry momenta

$$\begin{aligned} \Gamma &: (0, 0, 0), & X &: (\pi, 0, 0), & M &: (\pi, \pi, 0) \\ Z &: (0, 0, \pi), & R &: (\pi, 0, \pi), & A &: (\pi, \pi, \pi). \end{aligned}$$

and plot the energy bands along the high-symmetry line $\Gamma - X - M - \Gamma - Z - R - A - Z$. Let us start with the $m = 0$ limit. As shown in Fig. 6(b), the low-energy bands are quasi-1D around the $k_z = 0$ plane, which is consistent with the picture of decoupled helical modes explained below Eq. (C1). A small finite $m > 0$ drives the system to a nodal line semi-metal phase, as illustrated in Fig. 6(c). The nodal line is protected by the $P\widetilde{T}$ symmetry and pinned in the $k_z = 0$ plane by the glide symmetry

$\widetilde{M}_z = \{m_{001} | \frac{1}{2} \frac{1}{2} 0\}$. When m increases, the nodal line shrinks towards the Γ point (Fig. 6(d-g)). At a critical value $m = 2\gamma$, the nodal line shrinks to a point at Γ (Fig. 6(h)). Further increasing m will open a gap (Fig. 6(i)). This gap is trivial since it is adiabatically connected to the $m \rightarrow \infty$ limit, which describes an atomic insulator with dimers formed by nearest neighbors. Now let us discuss the $m < 0$ case. Rather similarly, a small $-2\gamma < m < 0$ also drives the system to a nodal-line semi-metal, whose nodal-line is pinned on the $k_z = 0$ plane and shrinks as $|m|$ increases, finally becoming the Γ point when $m = -2\gamma$. Tuning m to $-2\gamma - \epsilon$, where ϵ is a small positive number, will also open a gap when $t > \gamma$. However, this state is not adiabatically connected to the $m \rightarrow -\infty$ limit. To see this, notice that when $k_z = \pi + \delta k_z$, $\delta k_z \ll \pi$, the first row of Eq. (C1) can be expanded as $(m + 4t - t\delta k_z^2)\rho_x\tau_x\sigma_x - 2t\delta k_z\rho_z\tau_z\sigma_z$, which defines four pairs of chiral and anti-chiral states near $k_z = \pi$ when $m + 4t$ is small (see the explanation below Eq. (C1)). Similar to the above discussions, the band structure is quasi-1D on $k_z = \pi$ when $m = -4t$, and is a nodal-line semi-metal with a nodal line pinned on the $k_z = \pi$ plane when $0 < |m + 4t| < 2\gamma$. In this paper, we take $t = 2 > \gamma = 1$, which means there are no overlap between the two gapless regions $|m| < 2\gamma$ and $|m + 4t| < 2\gamma$. Since the low energy physics of the above two nodal-line semi-metals are similar to each other, an intrinsic STI phase should emerge near $k_z = \pi$, when $|m + 4t| \ll \gamma$ and C_4T preserving disorder is introduced, similar to intrinsic STI phase near $k_z = 0$ when $|m| \ll \gamma$, as illustrated in Fig. 2(b) of the main text. Since our purpose is to demonstrate the existence of an intrinsic STI phase, we will focus on $|m| \ll \gamma$ and $k_z \approx 0$ in following discussions and numerical calculations.

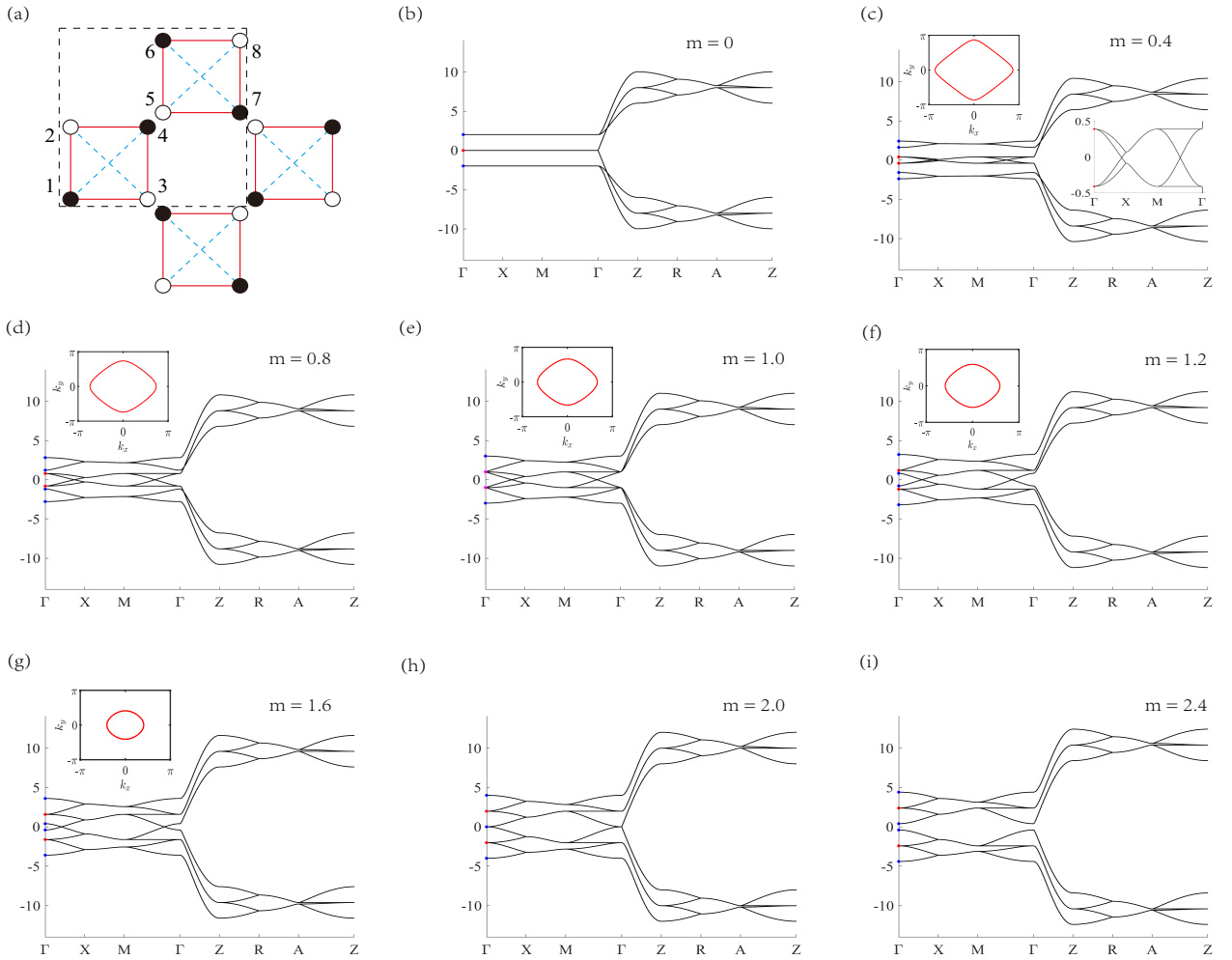


FIG. 6. (a). The lattice model with eight orbitals per unit cell. Orbitals 6, 7, 8 in unit cells (010), (100), and (110) (rather than that in home unit cells) are shown for the convenience of illustration. In each cell, $\rho = \pm 1$ labels a square (e.g. $\rho = 1 \rightarrow$ sites $\{1, 2, 3, 4\}$), $\tau = \pm 1$ labels a column (e.g. $\rho = 1, \tau = 1 \rightarrow$ sites $\{1, 2\}$), and $\sigma = \pm 1$ labels a site (e.g. $\rho = 1, \tau = 1, \sigma = 1 \rightarrow$ site 1). (b-i). The band structure of the lattice model with $t = 2, \gamma = 1, \lambda = 0.01$ and different m . Upper left insets of (c-g) show the position of the nodal-line on the $k_z = 0$ plane. Right inset of (c) shows the details of low-energy band structure at $k_z = 0$. Blue and red dots at Γ label C_2 eigenstates with eigenvalue ± 1 respectively. When $m \ll \gamma$, the low energy band structure is dominated by the $C_2 = -1$ sector.

2. Low energy states

When m is zero, low energy states are the quasi-1D helical modes around $k_z = 0$. In this subsection, we will derive a low energy \mathbf{k} -p expansion for the helical modes. For a finite but small m , these modes form a nodal line semi-metal. We will also discuss the transition from the nodal line semi-metal to a trivial band insulator when m becomes larger.

We view $H(k_z = 0)$ as a 2D Hamiltonian. When $m = 0$, it decomposes into decoupled molecules on the red squares shown in Fig. 6(a). The Hamiltonian around $k_z = 0$ reduces to

$$\begin{aligned}
 H(\mathbf{k}) &= 2tk_z \cdot \rho_z \tau_z \sigma_z + \rho_0 \begin{pmatrix} 0 & \gamma e^{i\frac{k_y}{2}} & \gamma e^{i\frac{k_x}{2}} & \lambda e^{i\frac{k_x+k_y}{2}} \\ \gamma e^{-i\frac{k_y}{2}} & 0 & \lambda e^{i\frac{k_x-k_y}{2}} & \gamma e^{i\frac{k_x}{2}} \\ \gamma e^{-i\frac{k_x}{2}} & \lambda e^{-i\frac{k_x-k_y}{2}} & 0 & \gamma e^{i\frac{k_y}{2}} \\ \lambda e^{-i\frac{k_x+k_y}{2}} & \gamma e^{-i\frac{k_x}{2}} & \gamma e^{-i\frac{k_y}{2}} & 0 \end{pmatrix} + \mathcal{O}(k_z^2) \\
 &= 2tk_z \cdot \rho_z \tau_z \sigma_z + \rho_0 \cdot \text{diag}(1 \ e^{i\frac{k_y}{2}} \ e^{i\frac{k_x}{2}} \ e^{i\frac{k_x+k_y}{2}})^\dagger \cdot \begin{pmatrix} 0 & \gamma & \gamma & \lambda \\ \gamma & 0 & \lambda & \gamma \\ \gamma & \lambda & 0 & \gamma \\ \lambda & \gamma & \gamma & 0 \end{pmatrix} \cdot \text{diag}(1 \ e^{i\frac{k_y}{2}} \ e^{i\frac{k_x}{2}} \ e^{i\frac{k_x+k_y}{2}}) + \mathcal{O}(k_z^2), \quad (\text{C15})
 \end{aligned}$$

where the \mathbf{k} -independent matrix in the middle represent the local Hamiltonian of each molecule. We find the eigenvectors and eigenvalues at $k_z = 0$:

$$u_{\xi=-1, \eta=\pm 1, n=1}(\mathbf{k}) = \frac{1}{2} \begin{pmatrix} \frac{1+\eta}{2} \\ \frac{1-\eta}{2} \cdot e^{i\frac{k_x+k_y}{2}} \end{pmatrix} \otimes \begin{pmatrix} 1 \\ ie^{-i\frac{k_y}{2}} \\ -ie^{-i\frac{k_x}{2}} \\ -e^{-i\frac{k_x+k_y}{2}} \end{pmatrix}, \quad E = -\lambda, \quad (\text{C16})$$

$$u_{\xi=-1, \eta=\pm 1, n=2}(\mathbf{k}) = \frac{1}{2} \begin{pmatrix} \frac{1+\eta}{2} \\ \frac{1-\eta}{2} \cdot e^{i\frac{k_x+k_y}{2}} \end{pmatrix} \otimes \begin{pmatrix} 1 \\ -ie^{-i\frac{k_y}{2}} \\ ie^{-i\frac{k_x}{2}} \\ -e^{-i\frac{k_x+k_y}{2}} \end{pmatrix}, \quad E = -\lambda, \quad (\text{C17})$$

$$u_{\xi=1, \eta=\pm 1, n=1}(\mathbf{k}) = \frac{1}{2} \begin{pmatrix} \frac{1+\eta}{2} \\ \frac{1-\eta}{2} \cdot e^{i\frac{k_x+k_y}{2}} \end{pmatrix} \otimes \begin{pmatrix} 1 \\ -e^{-i\frac{k_y}{2}} \\ -e^{-i\frac{k_x}{2}} \\ e^{-i\frac{k_x+k_y}{2}} \end{pmatrix}, \quad E = -2\gamma + \lambda, \quad (\text{C18})$$

$$u_{\xi=1, \eta=\pm 1, n=2}(\mathbf{k}) = \frac{1}{2} \begin{pmatrix} \frac{1+\eta}{2} \\ \frac{1-\eta}{2} \cdot e^{i\frac{k_x+k_y}{2}} \end{pmatrix} \otimes \begin{pmatrix} 1 \\ e^{-i\frac{k_y}{2}} \\ e^{-i\frac{k_x}{2}} \\ e^{-i\frac{k_x+k_y}{2}} \end{pmatrix}, \quad E = 2\gamma + \lambda. \quad (\text{C19})$$

Here $\eta = \pm 1$ indicates the $\rho_z = \pm 1$ block, $\xi = \pm 1$ is the C_2 ($= S_4^2$) eigenvalue of the molecule orbital. One can verify that these solutions satisfy

$$u_{\xi\eta n}(\mathbf{k} + \mathbf{G}) = V^\dagger(\mathbf{G})u_{\xi\eta n}(\mathbf{k}) \quad (\text{C20})$$

where $V(\mathbf{G})$ is the embedding matrix given in Eq. (C4).

We have chosen $\gamma \gg \lambda > 0$ such that $\xi = 1$ states have a large gap $\sim 4\gamma$ around the $k_z = 0$ plane provided $m = 0$. Low energy physics at $m = 0$ are hence dominated by the $\xi = -1$ states. We hence project the Dirac term $m\rho_x\tau_x\sigma_x + 2tk_z\rho_z\tau_z\sigma_z + \mathcal{O}(k_z^2)$ (given below Eq. (C1)) onto the $\xi = -1$ subspace. We obtain the effective Hamiltonian

$$\begin{aligned}
 H^{(\xi=-1)}(\mathbf{k}) &= -\lambda\rho_0\sigma_0 + 2tk_z\rho_z\sigma_x - m \cdot \text{Re}[f(\mathbf{k}) + g(\mathbf{k})]\rho_x\sigma_0 + m \cdot \text{Re}[f(\mathbf{k}) + g(\mathbf{k})]\rho_y\sigma_0 \\
 &\quad - m \cdot \text{Re}[f(\mathbf{k}) - g(\mathbf{k})]\rho_x\sigma_x + m \cdot \text{Im}[f(\mathbf{k}) - g(\mathbf{k})]\rho_y\sigma_x + \mathcal{O}(k_z^2), \quad (\text{C21})
 \end{aligned}$$

where $f(\mathbf{k}) = (1 + e^{i(k_x+k_y)})/4$, $g(\mathbf{k}) = (e^{ik_x} + e^{ik_y})/4$. We use $\rho_z = \pm 1$ for $\eta = \pm 1$ states and $\sigma_z = \pm 1$ for $n = 1, 2$ states, respectively, in the subspace of $\xi = -1$. Clearly, when $m = 0$, $H^{(\xi=-1)}$ represent two decoupled helical modes (per unit cell), consistent with the topological crystal construction in Fig. 1 of the main text. For $|m| \ll \gamma$, we can omit the coupling between $\xi = \pm 1$ subspaces. Then, the four energy bands in the $\xi = -1$ subspace are

$$-\lambda \pm 2\sqrt{t^2k_z^2 + m^2|f(\mathbf{k})|^2}, \quad -\lambda \pm 2\sqrt{t^2k_z^2 + m^2|g(\mathbf{k})|^2}. \quad (\text{C22})$$

Since $|f(\mathbf{k})| = 0$ iff $k_y = -k_x \pm \pi$, $|g(\mathbf{k})| = 0$ iff $k_y = k_x \pm \pi$, a nodal line crossing is formed along the square

$$(\pi, 0, 0) \rightarrow (0, \pi, 0) \rightarrow (-\pi, 0, 0) \rightarrow (0, -\pi, 0) \rightarrow (\pi, 0, 0). \quad (\text{C23})$$

Being protected the $P\tilde{T}$ symmetry, the nodal line is stable against coupling to the $\xi = 1$ subspace. However, we find that the coupling lifts the four-fold degeneracy at X, which is not protected by the single-valued magnetic space group P_{C4}/nbm , and eventually deforms the square-shaped nodal line into a circular shape (Fig. 6(c)-(g)).

For later convenience, we also derive the representation of P (Eq. (C6)) and S_4 (Eq. (C10)) at $\mathbf{k} = 0$ in the $\xi = -1$ subspace:

$$\mathcal{D}^{(\xi=-1)}(P) = -\rho_x \sigma_0, \quad \mathcal{D}^{(\xi=-1)}(S_4) = -i\rho_0 \sigma_z. \quad (\text{C24})$$

At $\mathbf{k} = 0$, the doubly degenerate energy level $-\lambda + m$ has P and S_4 eigenvalues 1, 1 and i , $-i$, respectively; and the other doubly degenerate level $-\lambda - m$ has P and S_4 eigenvalues -1 , -1 and i , $-i$, respectively.

The nodal line shrinks as m increases. As shown in Fig. 6, all the high symmetry momenta except Γ remain gapped as m changes from 0^+ to values greater than 2γ . A level crossing happens at Γ when $m = 2\gamma$, upon which the nodal line shrinks to zero. We now analyze this level crossing; it may help us understand the topology of the model. Thanks to the C_2 symmetry, the $\xi = \pm 1$ subspaces are decoupled at Γ . Each of the energy levels $E = -\lambda \pm 2m$ in the $\xi = -1$ subspace is a monotonous function of m , hence, provided $\gamma \gg \lambda > 0$, they do not participate in the level crossing around $\pm\lambda$ when $m = 2\gamma$. Thus, we only need to study the $\xi = +1$ subspace. The effective Hamiltonian on the basis $u_{\xi=+1, \eta, n}(\mathbf{0})$ reads

$$H^{(\xi=+1)}(\mathbf{k} = 0) = \lambda\rho_0\sigma_0 - 2\gamma\rho_0\sigma_z + m\rho_x\sigma_0. \quad (\text{C25})$$

The energy levels $\lambda + 2\gamma - m$ and $\lambda - 2\gamma + m$ cross each other at $m = 2\gamma$. We also notice that, at $\mathbf{k} = 0$, the P (Eq. (C6)) and S_4 (Eq. (C10)) symmetry operators act in the $\xi = +1$ subspace as

$$\mathcal{D}^{(\xi=+1)}(P) = \rho_x\sigma_0, \quad \mathcal{D}^{(\xi=+1)}(S_4) = -\rho_0\sigma_z. \quad (\text{C26})$$

One can immediately observe that the level $\lambda + 2\gamma - m$ has P and S_4 eigenvalues -1 and 1 , respectively, and the level $\lambda - 2\gamma + m$ has P and S_4 eigenvalues 1 and -1 , respectively.

We now calculate the symmetry-based indicators [13, 69, 55] given by P and S_4 eigenvalues:

$$\eta_{4I} = \sum_{\mathbf{k} \in K^8} n_{\mathbf{k}}(P = -1) \pmod{4}, \quad (\text{C27})$$

$$z_2 = \sum_{\mathbf{k} \in K^4} \frac{n_{\mathbf{k}}(S_4 = 1) - n_{\mathbf{k}}(S_4 = -1)}{2} \pmod{2}, \quad (\text{C28})$$

$$\delta_{2S} = \sum_{\mathbf{k} \in K^4} e^{ik_z} (n_{\mathbf{k}}(S_4 = -i) - n_{\mathbf{k}}(S_4 = -1)) \pmod{2}. \quad (\text{C29})$$

Here $K^8 = \{(0/\pi, 0/\pi, 0/\pi)\}$ are the eight inversion-invariant momenta, and $K^4 = \{(0, 0, 0/\pi), (\pi, \pi, 0/\pi)\}$ are the four S_4 -invariant momenta. $n_{\mathbf{k}}(P = -1)$, $n_{\mathbf{k}}(S_4 = \pm 1, \pm i)$ denote the number of occupied levels at \mathbf{k} that have the corresponding symmetry eigenvalues. For more details, as well as four additional indicators ($z_{2I, i}$, $z_{4S, \pi}$) representing 3D Chern numbers, readers may refer to discussions around Eqs. (235) and (270) of the supplementary materials of Ref. [69]. Since $z_{2I, i}$, $z_{4S, \pi}$ are always trivial in our model, we do not discuss them further here. Additionally, one need not worry about crossings enforced by the compatibility relations of $C_2 = S_4^2$, which would invalidate z_2, δ_{4S} , because there is no crossing along the high symmetry lines $\Gamma Z, MA, XR$. Thus, η_{4I} , z_2 , and δ_{2S} are all the meaningful indicators given by P and S_4 . Odd η_{4I} and δ_2 implies existence of Weyl points. In a gapped insulator there must be $\eta_4 \in \text{even}$, $\delta_{2S} = 0$ and

$$P_3 = \frac{\eta_{4I}}{4} = \frac{z_2}{2} \pmod{1} \quad (\text{C30})$$

provided all 3D Chern numbers equal to zero.

We now calculate $\eta_{4I}, z_2, \delta_{2S}$ for our model. Since the $m \rightarrow \infty$ limit must have trivial indicators, we can replace $n_{\mathbf{k}}$ in Eqs. (C27) to (C29) by $\delta n_{\mathbf{k}}$ - the change of $n_{\mathbf{k}}$ with respect to the $m \rightarrow \infty$ limit. According to the discussions around Eq. (C25), the nodal line semi-metal with $0 < m < 2\gamma$ has

$$\delta n_{\Gamma}(P = 1) = 1, \quad \delta n_{\Gamma}(P = -1) = -1, \quad \delta n_{\Gamma}(S_4 = 1) = -1, \quad \delta n_{\Gamma}(S_4 = -1) = 1, \quad \delta n_{\Gamma}(S_4 = \pm i) = 0. \quad (\text{C31})$$

and hence

$$\eta_{AI} = 3, \quad z_2 = 1, \quad \delta_{2S} = 1. \quad (\text{C32})$$

$\eta_{AI} = 3$ indicates that the considered state must have Weyl points. Similarly, $\delta_{2S} = 1$ also implies that the considered state must have Weyl points. Due to the $P\tilde{T}$ symmetry, these Weyl points must be part of nodal lines, which are further pinned in the $k_z = 0$ plane by the glide ($\tilde{M}_z = \{m_{001} | \frac{1}{2} \frac{1}{2} 0\}$) symmetry. It appears that the indicators only reveal the presence of nodal lines.

For negative m , we find

$$\begin{aligned} -2\gamma < m < 0: \quad & \delta n_\Gamma(P=1) = 3, \quad \delta n_\Gamma(P=-1) = -3, \quad \delta n_\Gamma(S_4=1) = -1, \quad \delta n_\Gamma(S_4=-1) = 1, \quad \delta n_\Gamma(S_4=\pm i) = 0 \\ & \Rightarrow \eta_{AI} = 1, \quad z_2 = 1, \quad \delta_{2S} = 1, \end{aligned} \quad (\text{C33})$$

$$\begin{aligned} -4t + 2\gamma < m < -2\gamma: \quad & \delta n_\Gamma(P=1) = 4, \quad \delta n_\Gamma(P=-1) = -4, \quad \delta n_\Gamma(S_4=\pm 1) = 0, \quad \delta n_\Gamma(S_4=\pm i) = 0 \\ & \Rightarrow \eta_{AI} = 0, \quad z_2 = 0, \quad \delta_{2S} = 0. \end{aligned} \quad (\text{C34})$$

Thus, the state with $-2\gamma < m < 0$ is a nodal line semi-metal as the $0 < m < 2\gamma$ case, and the band insulator with $-4t + 2\gamma < m < -2\gamma$ must have $P_3 = 0$ according to Eq. (C30).

3. Random fluxes or imaginary hoppings

As pointed out in the main text, one can introduce local gaps to the helical modes that only respect the C_4T symmetry on average. These gaps localize the low energy states in the bulk and give rise the intrinsic statistical topological insulator (STI) characterized by $P_3 = 1/2$. One choice of the local gap is random flux through the $2a$ and $2b$ Wyckoff positions. Consider the $m = 0$ limit, where the low energy Hamiltonian around $k_z = 0$ decomposes into decoupled helical modes (Eq. (C15)). In the xy plane, these helical modes are molecule states localized on the squares centered at the $2a$ positions. Each molecule has a local Hamiltonian:

$$H^{(\text{loc})}(k_z) = 2\eta t k_z \cdot \tau_z \sigma_z + \begin{pmatrix} 0 & \gamma e^{i\frac{\Phi}{4}} & \gamma e^{-i\frac{\Phi}{4}} & \lambda \\ \gamma e^{-i\frac{\Phi}{4}} & 0 & \lambda & \gamma e^{i\frac{\Phi}{4}} \\ \gamma e^{i\frac{\Phi}{4}} & \lambda & 0 & \gamma e^{-i\frac{\Phi}{4}} \\ \lambda & \gamma e^{-i\frac{\Phi}{4}} & \gamma e^{i\frac{\Phi}{4}} & 0 \end{pmatrix} + \mathcal{O}(k_z^2), \quad (\text{C35})$$

where Φ is a flux passing through the molecule, $\eta = 1, -1$ correspond to the molecule formed by orbitals 1, 2, 3, 4 and 5, 6, 7, 8, respectively. We have dropped the \mathbf{k} -dependent phase factors in Eq. (C15), which arise from the plane-wave-like Bloch basis, because we are now studying a local problem. The eigenstates at $k_z = 0$ are identical to those in Eqs. (C16)-(C19) except that the \mathbf{k} -dependent phase factors should be omitted here. Then we find that the low energy Hamiltonian in the $\xi = -1$ and $+1$ subspaces are

$$H^{(\text{loc}, \xi=-1)} = -\lambda \cdot \sigma_0 + 2\eta t k_z \cdot \sigma_x - 2\gamma \sin \frac{\Phi}{4} \cdot \sigma_z + \mathcal{O}(k_z^2) \quad (\text{C36})$$

and

$$H^{(\text{loc}, \xi=1)} = \lambda \cdot \sigma_0 + 2\eta t k_z \cdot \sigma_x - 2\gamma \cos \frac{\Phi}{4} \cdot \sigma_z + \mathcal{O}(k_z^2) \quad (\text{C37})$$

respectively. Clearly, a finite flux will gap the helical modes in the $\xi = -1$ sector.

We find it is more convenient to add random imaginary part to the γ term (red bonds in Fig. 6(a)). They introduce not only random fluxes, but also random hopping strengths. This disorder term can be written as

$$\begin{aligned} H^{(\text{dis})} = \sum_{\mathbf{R}} i & (w_{\mathbf{R},1} c_{\mathbf{R},1}^\dagger c_{\mathbf{R},2} + w_{\mathbf{R},2} c_{\mathbf{R},2}^\dagger c_{\mathbf{R},3} + w_{\mathbf{R},3} c_{\mathbf{R},3}^\dagger c_{\mathbf{R},1} + w_{\mathbf{R},4} c_{\mathbf{R},4}^\dagger c_{\mathbf{R},3} \\ & + w_{\mathbf{R},5} c_{\mathbf{R},5}^\dagger c_{\mathbf{R}+(010),6} + w_{\mathbf{R},6} c_{\mathbf{R},6}^\dagger c_{\mathbf{R},8} + w_{\mathbf{R},7} c_{\mathbf{R},7}^\dagger c_{\mathbf{R}-(100),5} + w_{\mathbf{R},8} c_{\mathbf{R},8}^\dagger c_{\mathbf{R}-(010),7}) + h.c. \end{aligned} \quad (\text{C38})$$

Here $w_{\mathbf{R},\alpha}$ are quenched gaussian variables satisfying

$$\langle w_{\mathbf{R},\alpha} w_{\mathbf{R}',\beta} \rangle = W^2 \cdot \delta_{\mathbf{R},\mathbf{R}'} \delta_{\alpha\beta}. \quad (\text{C39})$$

W is the parameter controlling the disorder strength. For $m = 0$, we expect the intrinsic STI phase at weak and intermediate W because small random fluxes are able to gap out the helical modes. The $W \rightarrow \infty$ limit must give the trivial Anderson insulator.

4. Uniform C_4T -breaking flux patterns

In the last subsection we argued that random local fluxes can gap out the helical modes and drive the system into an intrinsic STI phase. We find that our model could become a clean axion insulator (protected by S_4 or P) in the presence of a properly designed C_4T -breaking flux pattern.

We assume the translation symmetry and denote the fluxes through the squares centered at $(\frac{1}{4}, \frac{1}{4}, 0)$, $(\frac{3}{4}, \frac{3}{4}, 0)$, $(\frac{1}{4}, \frac{3}{4}, 0)$, $(\frac{3}{4}, \frac{1}{4}, 0)$ and $\Phi_A, \Phi_B, \Phi_C, \Phi_D$, respectively (Fig. 7(a)). We consider two patterns

$$(I) : \quad \Phi_A = \Phi_B = -\Phi_C = -\Phi_D = \Phi, \quad (C40)$$

$$(II) : \quad \Phi_A = -\Phi_B = \Phi, \quad \Phi_C = \Phi_D = 0. \quad (C41)$$

Pattern-(I) respects both S_4 and P symmetries, whereas pattern-(II) only respects S_4 but breaks P . We find the corresponding Hamiltonians

$$\begin{aligned} H^{(I)}(\mathbf{k}) = & (m + 2t - 2t \cos k_z) \rho_x \tau_x \sigma_x + 2t \sin k_z \rho_z \tau_z \sigma_z \\ & + \gamma \cos \frac{\Phi}{4} \left(\cos \frac{k_x}{2} \rho_0 \tau_x \sigma_0 - \sin \frac{k_x}{2} \rho_0 \tau_y \sigma_0 + \cos \frac{k_y}{2} \rho_0 \tau_0 \sigma_x - \sin \frac{k_y}{2} \rho_0 \tau_0 \sigma_y \right) \\ & + \gamma \sin \frac{\Phi}{4} \left(\sin \frac{k_x}{2} \rho_0 \tau_x \sigma_z + \cos \frac{k_x}{2} \rho_0 \tau_y \sigma_z - \sin \frac{k_y}{2} \rho_0 \tau_z \sigma_x - \cos \frac{k_y}{2} \rho_0 \tau_z \sigma_y \right) \\ & + \lambda \left(\cos \frac{k_x}{2} \cos \frac{k_y}{2} \rho_0 \tau_x \sigma_x + \sin \frac{k_x}{2} \sin \frac{k_y}{2} \rho_0 \tau_y \sigma_y - \sin \frac{k_x}{2} \cos \frac{k_y}{2} \rho_0 \tau_y \sigma_x - \cos \frac{k_x}{2} \sin \frac{k_y}{2} \rho_0 \tau_x \sigma_y \right), \quad (C42) \end{aligned}$$

$$\begin{aligned} H^{(II)}(\mathbf{k}) = & (m + 2t - 2t \cos k_z) \rho_x \tau_x \sigma_x + 2t \sin k_z \rho_z \tau_z \sigma_z \\ & + \gamma \cos \frac{\Phi}{4} \left(\cos \frac{k_x}{2} \rho_0 \tau_x \sigma_0 - \sin \frac{k_x}{2} \rho_0 \tau_y \sigma_0 + \cos \frac{k_y}{2} \rho_0 \tau_0 \sigma_x - \sin \frac{k_y}{2} \rho_0 \tau_0 \sigma_y \right) \\ & + \gamma \sin \frac{\Phi}{4} \left(\sin \frac{k_x}{2} \rho_z \tau_x \sigma_z + \cos \frac{k_x}{2} \rho_z \tau_y \sigma_z - \sin \frac{k_y}{2} \rho_z \tau_z \sigma_x - \cos \frac{k_y}{2} \rho_z \tau_z \sigma_y \right) \\ & + \lambda \left(\cos \frac{k_x}{2} \cos \frac{k_y}{2} \rho_0 \tau_x \sigma_x + \sin \frac{k_x}{2} \sin \frac{k_y}{2} \rho_0 \tau_y \sigma_y - \sin \frac{k_x}{2} \cos \frac{k_y}{2} \rho_0 \tau_y \sigma_x - \cos \frac{k_x}{2} \sin \frac{k_y}{2} \rho_0 \tau_x \sigma_y \right). \quad (C43) \end{aligned}$$

$\gamma \cos \frac{\Phi}{4}$ replace the γ parameter in Eq. (C1), and the $\gamma \sin \frac{\Phi}{4}$ terms are new. Symmetry-based indicators $\eta_{4I}, z_2, \delta_{2S}$ (Eqs. (C27) to (C29)) can be easily computed, and they suggest a phase diagram shown in (Fig. 7(b)). $H^{(I)}$ and $H^{(II)}$ happen to have the same phase diagram, but their gapless phases are physically different. Gapless phase in $H^{(I)}$ is a nodal line semi-metal due to the $\bar{M}_z = \{m_{001} | \frac{1}{2} \frac{1}{2} 0\}$ symmetry, whereas the gapless phase in $H^{(II)}$ is a Weyl semi-metal.

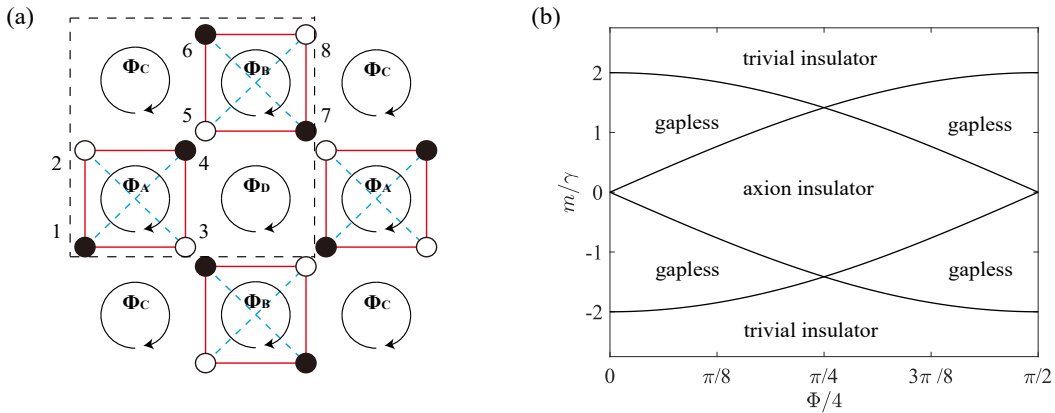


FIG. 7. (a) The position of the four fluxes $\Phi_A, \Phi_B, \Phi_C, \Phi_D$. (b) Phase diagram in the presence of C_4T -breaking flux patterns. $0 < \gamma < t$ is assumed for simplicity. Patterns (I) and (II) have the same phase diagram, but the gapless phases in the two patterns are physically different.

The phase diagram in Fig. 7(b) may suggest that our model (Eq. (C1)) is relatively “close” to a clean axion insulator. Perturbatively breaking C_4T symmetry drives the gapless system into a clean axion insulator protected by S_4 or P . However, the intrinsic STI protected by C_4T does *not* require the existence of (average or exact) S_4 or P .

D. Numerical methods and results

1. Quasi-1D localization length and the transfer matrix method

The quasi-1D localization length ξ_{1D} is a commonly used quantity to determine the localization behavior of 2D or 3D systems [58, 59]. We focus on 3D systems in the following, while the 2D case is in principle similar. $\xi_{1D}(L)$ is defined for a sample with a quasi-1D shape (for example, with geometry $M \times L \times L$ where $M \gg L$), and reflects the slowest decay rate of energy eigenstates in the longitudinal direction. Since a quasi-1D sample can be viewed as a 1D system with many internal degrees of freedom, and electrons always localize in a 1D system with arbitrary non-zero disorder strength, $\xi_{1D}(L)$ always converges to a finite value when $M \rightarrow \infty$ with the exception of a perfectly clean sample. The (de)localization of a normal shaped sample, whose sizes in different directions are comparable, can be inferred from the scaling behavior of the dimensionless normalized quasi-1D localization length $\Lambda(L) = \xi_{1D}(L)/L$. For a metallic normal shaped sample of size $L \times L \times L$, its 3D localization length $\xi_{3D}(L)$ is much larger than L when L is sufficiently large. If the sample is prepared in a quasi-1D shape with longitudinal size $M \gg L$, $\xi_{1D}(L)$ grows faster than L , so $\Lambda(L) \rightarrow \infty$ as $L \rightarrow \infty$. In contrast, for a localized phase, $\xi_{3D}(L)$ converges to a finite value ξ_0 as $L \rightarrow \infty$. In this case, $\xi_{1D}(L)$ also converges to ξ_0 in the large L limit, leading to $\Lambda(L) \rightarrow 0$. For the critical state, $\xi_{1D}(L)$ increases linearly with L for large L , meaning that $\Lambda(L)$ approaches a finite value Λ_c when $L \rightarrow \infty$.

The transfer matrix method [58] is widely used to numerically compute $\xi_{1D}(L)$. A quasi-1D sample is divided into layers normal to the longitudinal direction, with the amplitudes of energy eigenstates on different layers related by the time-independent Schrödinger equation. Specifically, the Hamiltonian of a tight binding lattice model can be written as

$$H = \sum_{ij} t_{ij} c_i^\dagger c_j = \sum_{q=-r_1}^{r_2} \sum_{l=1}^M \sum_{\alpha, \beta=1}^s t_{l\alpha, (l+q)\beta} c_{l\alpha}^\dagger c_{(l+q)\beta} \quad (D1)$$

where i, j denote orbitals, l denotes layers and $1 \leq \alpha, \beta \leq s$ denote the s degrees of freedoms within each layer. The condition $r_1 \leq q \leq r_2$ implies that orbitals in the l th layer can hop to at most the $(l-r_1)$ th or $(l+r_2)$ th layer in one step. Since the transfer matrices have dimensions $(r_1 + r_2)s$ (see below), the division into layers should be carefully designed to minimize r_1, r_2 and s for optimal numerical efficiency. x direction is taken as the longitudinal direction for the lattice model introduced in Sec. C. Each layer consists of two orbitals in one ‘‘column’’ of a square, along with their partners generated by lattice translations in y, z directions. For example, orbitals $\{3, 4\}$ in Fig. 6(a), while orbitals $\{5, 6\}$ form the next layer. In this setup, $r_1 = r_2 = 1$ and $s = 2L^2$. The following derivation assumes $r_1 = r_2 = 1$ for simplicity.

The Schrödinger equation $H|\psi\rangle = E|\psi\rangle$ can be written as

$$\begin{aligned} \sum_{q=-1}^1 H_{l, l+q} \vec{\psi}_{l+q} &= E \vec{\psi}_l \\ \implies \vec{\psi}_{l+1} &= -H_{l, l+1}^{-1} ((H_{l, l} - E) \vec{\psi}_l + H_{l, l-1} \vec{\psi}_{l-1}) \end{aligned} \quad (D2)$$

where $(H_{l, l'})_{\alpha, \beta} = t_{l\alpha, l'\beta}$, and $\vec{\psi}_l^T = (\psi_{l,1}, \psi_{l,2}, \dots)$ are the amplitudes of an energy eigenstate with energy E in the l th layer. If $H_{l, l+1}$ is singular, a different layer partition with an invertible $H_{l, l+1}$ must be used. The relation between amplitudes in adjacent layers is:

$$\begin{bmatrix} \vec{\psi}_{l+1} \\ \vec{\psi}_l \end{bmatrix} = T_l \begin{bmatrix} \vec{\psi}_l \\ \vec{\psi}_{l-1} \end{bmatrix} \quad (D3)$$

where

$$T_l = \left[\begin{array}{c|c} -H_{l, l+1}^{-1} (H_{l, l} - E) & -H_{l, l+1}^{-1} H_{l, l-1} \\ \hline I_{s \times s} & 0_{s \times s} \end{array} \right] \quad (D4)$$

is the l th transfer matrix. In a disordered system, T_l 's contain random elements, and their consecutive product $O_M = \prod_{l=1}^M T_l$ transforms the amplitudes on the first two layers to those on the last two layers. A theorem by Oseledec [73] guarantees the existence of the limit $P = \lim_{M \rightarrow \infty} (O_M^\dagger O_M)^{1/2}$, whose eigenvalues $\{\exp(\nu_1), \exp(-\nu_1), \dots, \exp(\nu_s), \exp(-\nu_s)\}$ come in pairs. The positive exponents $\nu_1 > \dots > \nu_i > \nu_{i+1} > \dots > \nu_s > 0$ are called Lyapunov exponents (LEs). An eigenvector $\vec{\eta}_i$ of P with eigenvalue $\exp(-\nu_i)$ satisfies $\|O_M \vec{\eta}_i\|^2 = \|\exp(-M\nu_i) \vec{\eta}_i\|^2$ for sufficiently large M . Therefore, the smallest LE ν_s determines the slowest decay rate of energy eigenstates with energy E along the longitudinal direction, and the quasi-1D localization length is defined as $\xi_{1D} = 1/(\nu_s l_0)$, where $l_0 = 4$ for the lattice model denotes the number of layers in a unit cell.

In practice, the matrix O_M cannot be computed directly. This is because when M is large, $\exp(M\nu_i) \gg \exp(M\nu_j)$ for $\nu_i > \nu_j$, and the smallest LE will quickly pick up large round-off error since most computational resources are consumed by the large LEs. To overcome this difficulty, we perform a QR decomposition after each q transfer matrices are multiplied:

$$Q_j R_j = T_{qj} T_{qj-1} \dots T_{q(j-1)+1} Q_{j-1} \quad (\text{D5})$$

where $Q_j^\dagger Q_j = I$, $Q_0 = I_{2s \times 2s}$, and R_j is upper-triangular. The process is repeated for $j = 1, \dots, M/q$. During each step, the logarithms of diagonal elements of each R_j are stored. We point out without proof that [58]

$$\nu_i = \lim_{M/q \rightarrow \infty} \frac{1}{M/q - n_0} \sum_{j=n_0+1}^{M/q} \frac{\ln(R_j)_{i,i}}{q} \quad (\text{D6})$$

where we have excluded the first $n_0 q$ layers to avoid possible boundary effects.

Eq. (D6) also provides us an unbiased estimation of the numerical precision of LEs: each LE can be viewed as an average of $M/q - n_0$ random samples, whose standard derivation can be estimated and interpreted as the numerical error of the LE. Prudent readers may suspect that the ‘‘random samples’’ $\ln(R_j)_{i,i}/q$ with close i 's might not be independent for small q . In practice, we group up $r \sim 10$ adjacent ‘‘random samples’’ together and assume that different groups are independent.

We have introduced the method to calculate ν_s and its numerical precision $\delta\nu_s$ for a quasi-1D sample with a given disorder configuration. To further reduce the numerical uncertainty, we take the average of ν_s for N_D different disorder configurations. The averaged $\bar{\nu}_s$ and its uncertainty is given by

$$\bar{\nu}_s = \frac{1}{N_D} \sum_{k=1}^{N_D} \nu_s^{(k)}, \delta\bar{\nu}_s = \frac{1}{N_D} \sqrt{\sum_{k=1}^{N_D} (\delta\nu_s^{(k)})^2} \quad (\text{D7})$$

where $\nu_s^{(k)}$, $1 \leq k \leq N_D$ denotes ν_s for the k th disorder configuration. Numerical Λ 's in this paper are obtained by using $L \leq 40$, $M = 2.5 \times 10^4$, $N_D = 16$, $q = 4$, $r = 10$ and $n_0 = 100$. The precision of $\Lambda = 1/(\bar{\nu}_s l_0 L)$ reaches $\delta\Lambda/\Lambda \leq 0.6\%$ for systems with periodic boundary conditions in both y and z directions, and $\delta\Lambda/\Lambda \leq 1.5\%$ for systems with open boundary condition in z direction and periodic boundary condition in y direction.

2. Scaling analysis and Polynomial fitting of Λ

As mentioned above, $\Lambda(L)$ converges to a finite value Λ_c when $L \rightarrow \infty$ for a critical state. Therefore, $\Lambda(L)$ should be scale invariant for large L 's at a metal-insulator phase transition point. On the insulating side of the phase transition, the 3D localization length ξ_{3D} diverges as $\xi_{3D} \sim \tilde{r}^{-\nu}$, where $\tilde{r} = |r - r_c|/r_c$, r is a tuning parameter controlling the phase transition (not necessarily the disorder strength), and r_c is the critical value of r . The phase transition is characterized by a universal critical exponent $\nu > 0$, which only depends on the universality class. For sufficiently large L , Λ follows the one-parameter scaling law with scaling variable L/ξ_{3D} [59], which requires that

$$\Lambda(r, L) = f(L/\xi_{3D}(r)) = F(\tilde{r}L^{1/\nu}) \quad (\text{D8})$$

where f is the one-parameter scaling function. However, numerically accessible L 's for 3D models are generally not large enough for us to neglect the finite size effects associated to the irrelevant scaling variables in the renormalization group (RG) theory, where the metal-insulator transition is described by a saddle-point fixed point with one relevant scaling variable and multiple irrelevant scaling variables. The relevant scaling variable $\phi(\tilde{r}, L)$ has scaling dimension $1/\nu > 0$, while the irrelevant scaling variables all have negative scaling dimensions. For simplicity, we neglect all irrelevant variables but the least irrelevant one, i.e., the one with the largest scaling dimension $y < 0$, which is denoted $\psi(\tilde{r}, L)$. This approximation is justified by a relatively small irrelevant contribution to Λ and a large $|y|$ (see below). Considering the irrelevant contribution and the non-linearity of variables ϕ and ψ in \tilde{r} , Eq. (D8) is modified to [60]

$$\Lambda(r, L) = F(\phi(\tilde{r}, L), \psi(\tilde{r}, L)) \quad (\text{D9})$$

which can be Taylor expanded as

$$\Lambda(r, L) = \sum_{j_1=0}^{n_1} \sum_{j_2=0}^{n_2} a_{j_1, j_2} \phi(\tilde{r}, L)^{j_1} \psi(\tilde{r}, L)^{j_2} \quad (\text{D10})$$

where $\phi(\tilde{r}, L) = u_1(\tilde{r})L^{1/\nu}$, $\psi(\tilde{r}, L) = u_2(\tilde{r})L^{-y}$. When \tilde{r} is small, $u_1(\tilde{r})$ and $u_2(\tilde{r})$ can be further expanded as

$$u_i(\tilde{r}) = \sum_{j=0}^{m_i} b_{ij} \tilde{r}^j, i = 1, 2 \quad (\text{D11})$$

Since $\tilde{r} = 0$ corresponds to the phase transition point, $u_1(0) = 0$, which implies $b_{10} = 0$. We also require $a_{10} = a_{01} = 1$ to remove the ambiguity when defining u_1, u_2 . Unknown parameters in the above expansion scheme include a_{ij}, b_{ij}, r_c, ν and y , with total number

$$N_p = m_1 + m_2 + (n_1 + 1)(n_2 + 1) + 2 \quad (\text{D12})$$

The phase transition point r_c and the universal exponent ν are obtained by fitting the N_p parameters to numerical Λ 's using the χ^2 fitting method, which minimizes the residual

$$\chi^2 = \sum_{j=1}^{N_d} \left(\frac{\Lambda_j - F_j}{\delta\Lambda_j} \right)^2 \quad (\text{D13})$$

where $j = 1, \dots, N_d$ denotes N_d data points, F_j denotes the value obtained from Eq. (D10), and Λ_j and $\delta\Lambda_j$ denote numerical Λ 's and their numerical error. The goodness of fit P is given by [60]

$$P = 1 - \frac{1}{\Gamma(N_{DOF}/2)} \int_0^{\chi_{min}^2/2} \exp(-t) t^{N_{DOF}/2 - 1} dt \quad (\text{D14})$$

where $N_{DOF} = N_d - N_p$, and χ_{min}^2 is the minimal value of χ^2 . P is the probability that N_d data points randomly sampled from F_j with standard derivations $\delta\Lambda_j$ give a larger χ^2 than χ_{min}^2 . We require $P \geq 0.1$ for a fit to be acceptable. To avoid overfitting, we also require $N_d > 4N_p$ and the irrelevant contribution to $F(\tilde{r}, L)$ (sum of terms with $j_2 > 0$ in Eq. (D10)) to be small compared with F_j , which includes both the relevant and irrelevant contributions.

The error bars of the fitting parameters are determined using the Monte-Carlo method. This is done by generating synthetic data sets $\tilde{\Lambda}_j'$, which are Gaussian random numbers with expectation values given by fitted F_j 's, and standard derivations given by $\delta\Lambda_j$'s. We then fit Eq. (D10) to these synthetic data sets to obtain additional parameter sets. The degree of certainty of the fitting parameters are estimated as their respective 95% confidence intervals from 1000 different synthetic data sets.

We have focused on the polynomial fitting of Taylor expansions of $\Lambda(r, L)$ in above discussions. Since Λ is scale invariant at the phase transition point, fittings using Taylor expansions of $\Lambda, 1/\Lambda$ and $\ln \Lambda$ near the phase transition point are all in principle equivalent, provided that $\delta\Lambda/\Lambda$ is sufficiently small for the χ^2 fitting method to be well justified. In practice, one should choose the best fit with an acceptable goodness of fit, low expansion orders, small irrelevant contributions, and good numerical stability. Most of the phase transition points in Fig. 2(d) in the main text are determined by fitting Λ , while some are determined by fitting $1/\Lambda$, as will be discussed in the next section.

3. Numerical results

Let us first discuss the Fermi energy used in the calculation of Λ . As mentioned in the main text, we focus on the behavior of the model at the half-filled Fermi energy, with four electrons per unit cell. As discussed in Sec. C2, this corresponds to $E_F = -\lambda$ for $m = 0$, and a m -dependent E_F for $m \neq 0$. However, when $|m| \ll \gamma$, the m dependence of E_F arises from couplings between subspaces with different C_2 eigenvalues, which involve high energy bands and is thus very weak. In this work, we keep $t = 2, \gamma = 1, \lambda = 0.01$ fixed. As shown in Fig. 2(d) in the main text, the intrinsic STI phase occurs only when $|m| < 0.05$. It is explicit to numerically check that under these conditions, the difference between the half-filled Fermi energy (of the clean model) E_F and $-\lambda$ satisfies $|E_F + \lambda| < 1.25 \times 10^{-5}$, which is much smaller than any of the model parameters. Since such a small difference does not significantly change the phase boundary between the intrinsic STI and metal phases, we use $E_F = -\lambda = -0.01$ in all numerical calculations for simplicity.

We have shown the raw data and polynomial fitting of Λ used to determine the phase boundary near $m = 0.01, W_{c2} \approx 1.125$ in Fig. 2(c) of the main text. The Taylor expansion orders are chosen as $\{m_r, n_r, m_i, n_i\} = \{3, 2, 0, 1\}$. $N_p = 11$ parameters are used to fit $N_d = 96$ data points, yielding $N_{DOF} = N_d - N_p = 85$. The minimum residual is $\chi_{min}^2 = 70.30$, resulting in $\chi_{min}^2/N_{DOF} = 0.83$ and a goodness of fit $P = 0.71$. The optimal fit gives $W_{c2} = 1.125[1.015, 1.162], \nu = 1.40[1.24, 1.56]$, and $y = -2.67[-4.07, -1.40]$, where brackets denote 95% confidence intervals. Notably, the relevant contributions to Λ (red dots) are close to the fitted values (lines with different colors), indicating that the irrelevant contributions are small. This small irrelevant correction, together with a relatively large $|y|$, justifies neglecting scaling variables more irrelevant than ψ in Eq. (D9).

To obtain the phase diagram in Fig. 2(d) of the main text, both W and m are used to control the phase transition. Since the models with $m > 0$ and $m < 0$ are not related to each other by symmetry, their phase boundaries must be determined separately. Additionally, it turns out that near some points on the phase boundary, fitting $1/\Lambda$ is more suitable than fitting Λ . For completeness, here we present examples of fitting. In Fig. 8(a), with $m = -0.01$ fixed, W controls the phase transition. Polynomial fitting of Λ using $\{m_r, n_r, m_i, n_i\} = \{3, 2, 0, 1\}$ gives $W_{c2} = 1.135[0.982, 1.180]$ and $\nu = 1.48[1.25, 1.77]$ with $P = 0.96$. In Fig. 8(b), $W = 0.50$ is fixed, and m controls the phase transition. Polynomial fitting of Λ with $\{m_r, n_r, m_i, n_i\} = \{1, 3, 2, 1\}$ gives $m_c = 0.0255[0.0232, 0.0273]$ and $\nu = 1.32[1.20, 1.48]$ with $P = 0.99$. We note that another fit with slightly lower expansion order $\{m_r, n_r, m_i, n_i\} = \{1, 3, 1, 1\}$ may also be considered acceptable (Fig. 8(c)), yielding $m_c = 0.0271[0.0232, 0.0292]$, $\nu = 1.15[1.08, 1.25]$, and $P = 0.93$. The critical exponent ν from this fit is inconsistent with the previously reported value $\nu = 1.443[1.437, 1.449]$ for 3D Anderson transitions in the unitary universality class. We attribute this discrepancy to large finite size effects, evidenced by the relatively large irrelevant contribution. However, m_c from Fig. 8(b) and (c) are consistent with each other, suggesting that the estimation of m_c and the phase boundary is less affected by finite size effects. Finally, Fig. 8(d) shows the phase transition near $m = 0.01$, $W_{c1} = 0.171$. The fit using $1/\Lambda$ rather than Λ with expansion orders $\{m_r, n_r, m_i, n_i\} = \{4, 2, 1, 1\}$ yields $W_c = 0.171[0.159, 0.184]$, $\nu = 1.32[1.20, 1.45]$ with $P = 1.00$.

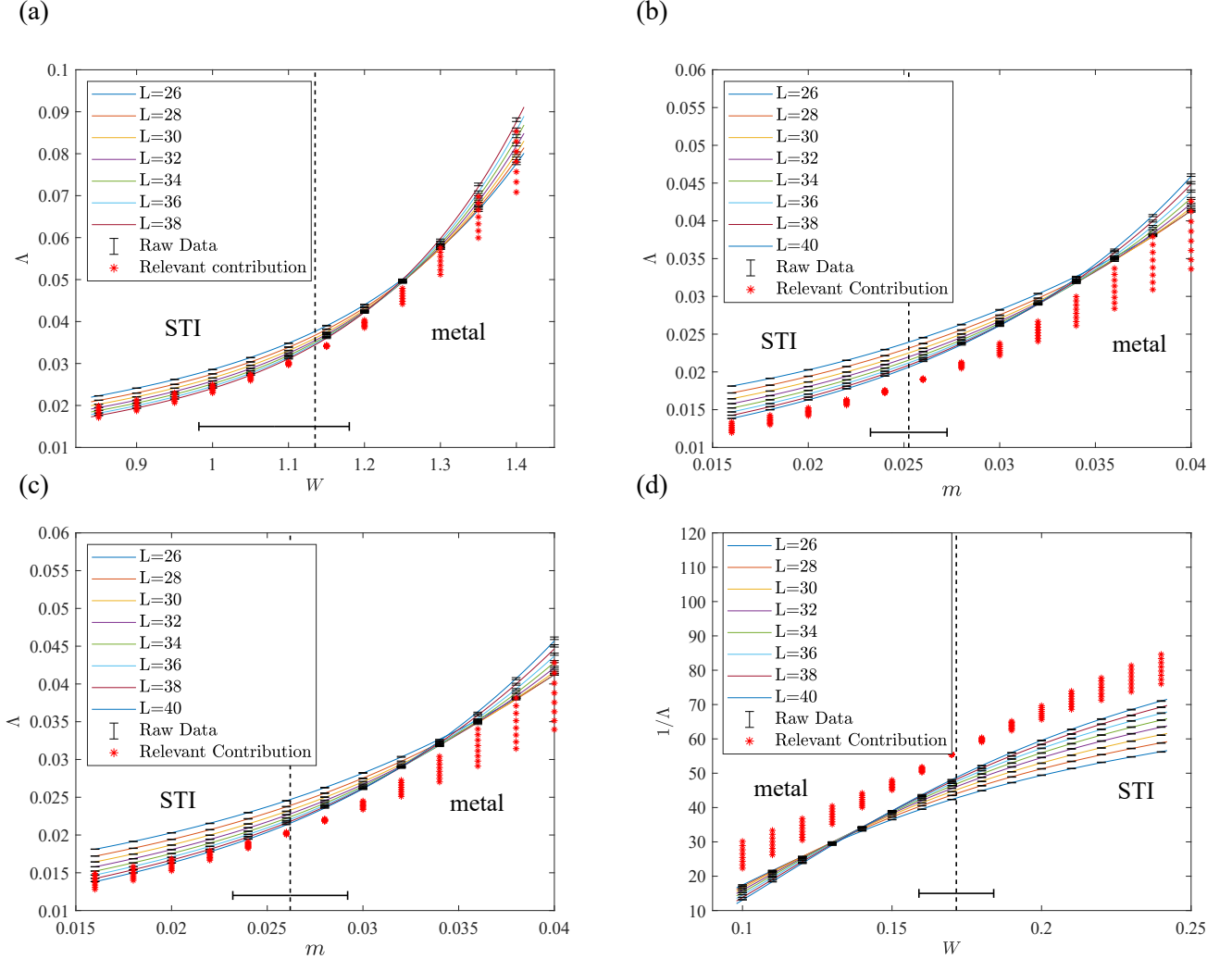


FIG. 8. Examples of other numerical data and polynomial fittings used to determine the phase diagram. Black dots with error bars show raw data, lines with different colors show the polynomial fitting, and red dots show the relevant contributions. (a) $m = -0.01$ fixed, $W_{c2} \approx 1.135$ controls the phase transition. (b-c) $W = 0.50$ fixed, m controls the phase transition. (b) and (c) use same raw data but different expansion orders. Despite the discrepancy of the critical exponent ν as explained in the paragraph, their m_c 's are consistent with each other. (d) Polynomial fitting of $1/\Lambda$ with $m = 0.01$ fixed, and $W_{c1} \approx 0.171$ controls the phase transition.

E. Generalization to $(C_2T)^2 = -1$ symmetry

Now, we generalize our discussion to $(C_2T)^2 = -1$ symmetry following the topological crystal method. Since C_2T is an anti-unitary symmetry squaring to -1 , it can also protect Kramers' pairs and forbid the opening of symmetric gaps, ruling out the existence of certain clean TCIs. Consider the topological crystal illustrated in Fig. 9(a), which consists of layers of Chern insulators with the same Chern number C . There are $|C|$ pairs of chiral and anti-chiral modes on each C_2T axis. If C is even, a C_2T -symmetric gap is allowed on each C_2T axis due to the net chirality, resulting in a layered Chern insulator with even 3D Chern number $C \in 2\mathbb{Z}$. In contrast, when C is odd, Kramers' degeneracy forbids the opening of C_2T -symmetric gaps on the C_2T axes, so layered Chern insulators with odd 3D Chern numbers are forbidden by exact C_2T symmetry. Introducing disorder on the hinges which breaks C_2T exactly but preserves it on average will lift the Kramers' degeneracy and allow the C_2T axes with odd C be localized. We have assumed the normals of layered Chern insulators to be $\pm e_y$ in above discussions, while decorations of Chern insulators with normals $\pm e_x$ can be made similarly, offering two 3D Chern numbers C_x, C_y in total. Therefore, breaking $(C_2T)^2 = -1$ symmetry from exact to average enriches the classification of layered Chern insulators from $2\mathbb{Z} \times 2\mathbb{Z}$ to $\mathbb{Z} \times \mathbb{Z}$, with $C_x \in \text{odd}$ or $C_y \in \text{odd}$ cases being intrinsic STIs.

Similarly, consider the topological crystal illustrated in Fig. 9(b), which consists of layers of Chern insulators with opposite Chern numbers C and $-C$ for adjacent layers. The bubble equivalence illustrated in Fig. 9(c) adiabatically changes C by $\Delta C = 2n$ without breaking the C_2T symmetry, making $C \in \text{even}$ equivalent to $C = 0$, and $C \in \text{odd}$ equivalent to $C = 1$. Since $C = 0$ is obviously trivial, we only have to consider the $C = 1$ case. When $(C_2T)^2 = -1$ is exact, there is one pair of chiral and anti-chiral states on each C_2T axis, and the Kramers' degeneracy forbids the opening of a symmetric gap as discussed above. When average C_2T preserving disorder is introduced on the hinges, the C_2T axes can be localized, while the Chern insulators remain robust. The disordered construction resembles the one illustrated in Fig. 1(a) of the main text and forms an axion STI with $\bar{\theta} = \pi$. Therefore, average C_2T symmetry with $(C_2T)^2 = -1$ can also protect intrinsic axion STIs with a \mathbb{Z}_2 invariant similar to the $(C_4T)^4 = 1$ symmetry.

In summary, average $(C_2T)^2 = -1$ symmetry protects a $\mathbb{Z} \times \mathbb{Z} \times \mathbb{Z}_2$ STI classification, where the first two topological indices $C_{x,y}$ denote 3D Chern numbers along x and y directions, and the third one δ indicates axion STI when $C_x = C_y = 0, \delta = 1$. Since states denoted by $\{C_x, C_y, \delta\} = \{2m, 2n, 0\}$ are extrinsic STIs, the classification of intrinsic STIs protected by average $(C_2T)^2 = -1$ symmetry is $\mathbb{Z}_2 \times \mathbb{Z}_2 \times \mathbb{Z}_2$.

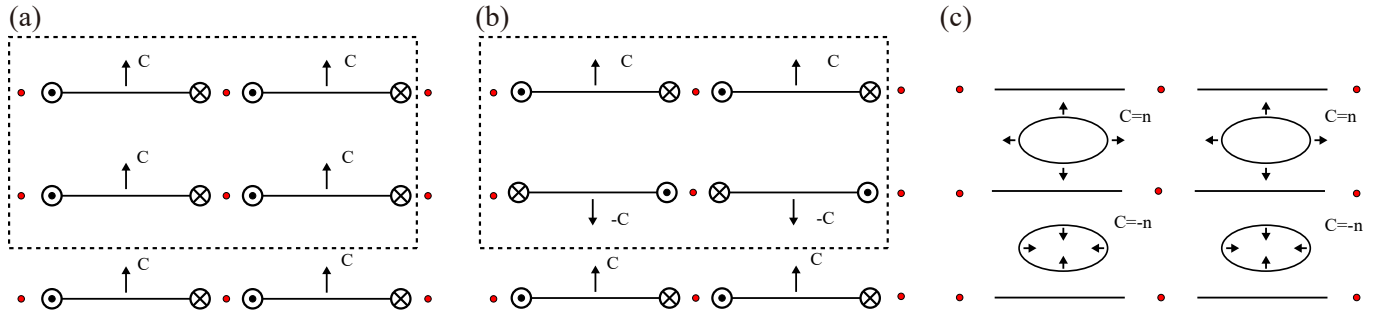


FIG. 9. Topological crystals with $(C_2T)^2 = -1$ symmetry. Red dots show the C_2T axes, which are occupied by intersecting hinges of Chern insulators. The dashed boxes show unit cells. (a) The topological crystal for layered Chern insulators. Those with $C \in \text{odd}$ can be insulating only in presence of disorder. (b) The topological crystal with opposite Chern numbers for adjacent layers. The $C = 1$ case become an intrinsic axion STI when average C_2T preserving disorder is introduced on the hinges. (c) By creating C_2T -symmetric Chern bubbles, a $\Delta C = 2n$ change can be realized adiabatically for the topological crystal illustrated in (b).